Draft version July 2, 2018
Typeset using LaTeX **twocolumn** style in AASTeX61

44 VALIDATED PLANETS FROM *K2* CAMPAIGN 10

John H. Livingston,[1,2,3] Michael Endl,[4] Fei Dai,[5,6] William D. Cochran,[4] Oscar Barragan,[7] Davide Gandolfi,[7] Teruyuki Hirano,[8] Sascha Grziwa,[9] Alexis M. S. Smith,[10] Simon Albrecht,[11] Juan Cabrera,[10] Szilard Csizmadia,[10] Jerome P. de Leon,[1] Hans Deeg,[12,13] Philipp Eigmüller,[10] Anders Erikson,[10] Mark Everett,[14] Malcolm Fridlund,[15,16] Akihiko Fukui,[17] Eike W. Guenther,[18] Artie P. Hatzes,[18] Steve Howell,[19] Judith Korth,[9] Norio Narita,[1,20,21,12] David Nespral,[12,13] Grzegorz Nowak,[12,13] Enric Palle,[12,13] Martin Pätzold,[9] Carina M. Persson,[16] Jorge Prieto-Arranz,[12,13] Heike Rauer,[10,22] Motohide Tamura,[1,20,21] Vincent Van Eylen,[15] and Joshua N. Winn[6]

[1] *Department of Astronomy, University of Tokyo, 7-3-1 Hongo, Bunkyo-ku, Tokyo 113-0033, Japan*
[2] *JSPS Fellow*
[3] livingston@astron.s.u-tokyo.edu
[4] *Department of Astronomy and McDonald Observatory, University of Texas at Austin, 2515 Speedway, Stop C1400, Austin, TX 78712, USA*
[5] *Department of Physics and Kavli Institute for Astrophysics and Space Research, Massachusetts Institute of Technology, Cambridge, MA, 02139, USA*
[6] *Department of Astrophysical Sciences, Princeton University, 4 Ivy Lane, Princeton, NJ 08544, USA*
[7] *Dipartimento di Fisica, Università di Torino, via P. Giuria 1, 10125 Torino, Italy*
[8] *Department of Earth and Planetary Sciences, Tokyo Institute of Technology, 2-12-1 Ookayama, Meguro-ku, Tokyo 152-8551, Japan*
[9] *Rheinisches Institut für Umweltforschung an der Universität zu Köln, Aachener Strasse 209, 50931 Köln, Germany*
[10] *Institute of Planetary Research, German Aerospace Center, Rutherfordstrasse 2, 12489 Berlin, Germany*
[11] *Stellar Astrophysics Centre, Department of Physics and Astronomy, Aarhus University, Ny Munkegade 120, DK-8000 Aarhus C, Denmark*
[12] *Instituto de Astrofísica de Canarias, C/ Vía Láctea s/n, 38205 La Laguna, Spain*
[13] *Departamento de Astrofísica, Universidad de La Laguna, 38206 La Laguna, Spain*
[14] *National Optical Astronomy Observatory, 950 North Cherry Avenue, Tucson, AZ 85719, USA*
[15] *Leiden Observatory, Leiden University, 2333CA Leiden, The Netherlands*
[16] *Department of Space, Earth and Environment, Chalmers University of Technology, Onsala Space Observatory, 439 92 Onsala, Sweden*
[17] *Okayama Astrophysical Observatory, National Astronomical Observatory of Japan, Asakuchi, Okayama 719-0232, Japan*
[18] *Thüringer Landessternwarte Tautenburg, Sternwarte 5, D-07778 Tautenberg, Germany*
[19] *Space Science and Astrobiology Division, NASA Ames Research Center, Moffett Field, CA 94035, USA*
[20] *Astrobiology Center, NINS, 2-21-1 Osawa, Mitaka, Tokyo 181-8588, Japan*
[21] *National Astronomical Observatory of Japan, NINS, 2-21-1 Osawa, Mitaka, Tokyo 181-8588, Japan*
[22] *Center for Astronomy and Astrophysics, TU Berlin, Hardenbergstr. 36, 10623 Berlin, Germany*

ABSTRACT

We present 44 validated planets from the 10$^{\rm th}$ observing campaign of the NASA *K2* mission, as well as high resolution spectroscopy and speckle imaging follow-up observations. These 44 planets come from an initial set of 72 vetted candidates, which we subjected to a validation process incorporating pixel-level analyses, light curve analyses, observational constraints, and statistical false positive probabilities. Our validated planet sample has median values of $R_p = 2.2\ R_\oplus$, $P_{\rm orb} = 6.9$ days, $T_{\rm eq} = 890$ K, and $J = 11.2$ mag. Of particular interest are four ultra-short period planets ($P_{\rm orb} \lesssim 1$ day), 16 planets smaller than 2 $R_\oplus$, and two planets with large predicted amplitude atmospheric transmission features orbiting infrared-bright stars. We also present 27 planet candidates, most of which are likely to be real and worthy of further observations. Our validated planet sample includes 24 new discoveries, and has enhanced the number of currently known super-Earths ($R_p \approx$ 1–2$R_\oplus$), sub-Neptunes ($R_p \approx$ 2–4$R_\oplus$), and sub-Saturns ($R_p \approx$ 4–8$R_\oplus$) orbiting bright stars ($J =$ 8–10 mag) by ∼4%, ∼17%, and ∼11%, respectively.

1. INTRODUCTION

The *K2* mission (Howell et al. 2014) is extending the *Kepler* legacy to a survey of the ecliptic plane, enabling the detection of transiting planets orbiting a wider range of host stars. The increased sky coverage of *K2* has enabled the detection of planets orbiting brighter host stars, as well as a larger selection of M dwarfs (Crossfield et al. 2016; Dressing et al. 2017; Hirano et al. 2018a). As a result, *K2* is yielding a large number of promising targets for follow-up studies (e.g. Vanderburg et al. 2015; Crossfield et al. 2015; Montet et al. 2015; Vanderburg et al. 2016a; Petigura et al. 2015; Vanderburg et al. 2016a,b,c; Crossfield et al. 2017). *K2* has also discovered planets in stellar cluster environments (Obermeier et al. 2016; Pepper et al. 2017; David et al. 2016b; Mann et al. 2016a, 2017; Gaidos et al. 2017; Ciardi et al. 2018), including one possibly still undergoing radial contraction (David et al. 2016a; Mann et al. 2016b).

We present here the results of our analysis of the *K2* photometric data collected during Campaign 10 (C10), along with a coordinated campaign of follow-up observations to better characterize the host stars and rule out false positive scenarios. Because of C10's relatively high galactic latitude, blending within the photometric apertures is less significant than for other fields, and contamination from background eclipsing binaries is low. We detect 72 planet candidates and validate 44 of them as *bona fide* planets using our observational constraints, 24 of which have not previously been reported in the literature. Our sample contains a remainder of 27 planet candidates, many of which are likely real planets.

The transit detections and follow-up observations that led to these discoveries were the result of an international collaboration called KESPRINT. Formed from the merger of two previously separate collaborations (KEST and ESPRINT), KESPRINT is focused on detecting and characterizing interesting new planet candidates from the *K2* mission (e.g. Fridlund et al. 2017; Guenther et al. 2017; Gandolfi et al. 2017; Niraula et al. 2017; Smith et al. 2018; Dai et al. 2017; Livingston et al. 2018; Hirano et al. 2018b; Van Eylen et al. 2018).

The rest of the paper is structured as follows. In Section 2 we describe our *K2* photometry and transit search. In Section 3 and Section 4 we describe our follow-up speckle imaging and high resolution spectroscopy of the candidates from our detection and vetting procedures. In Section 5 we describe our statistical validation framework and results. In Section 6 we discuss particular systems of interest, and we conclude with a summary in Section 7.

2. *K2* PHOTOMETRY AND TRANSIT SEARCH

Here we describe how we produce a list of vetted planet candidates from the pixel data telemetered from the *Kepler* spacecraft, as well as detailed light curve analyses. Throughout this paper we refer to stars by their nine digit EPIC IDs, and we concatenate these with two digit numbers to refer to planet candidates (ordered by orbital period).

2.1. *Photometry*

In C10, *K2* observed a ∼110 square degree field near the North Galactic cap from July 06, 2016 to September 20, 2016. Long cadence (30 minute) exposures of 28,345 target stars were downlinked from the spacecraft, and the data were calibrated and subsequently made available on the Mikulski Archive for Space Telescopes[1] (MAST). During the beginning of the campaign, a 3.5 pixel pointing error was detected and subsequently corrected six days after the start of observations. The data during this time is of substantially lower quality than the rest of the campaign, so we discard it in our analysis. An additional data gap was the result of the failure of detector module 4, which caused the photometer to power off for 14 days.

2.2. *Systematics*

Following the loss of two of its four reaction wheels, the *Kepler* spacecraft has been operating as *K2* (Howell et al. 2014). The dominant systematic signal in *K2* light curves is caused by the rolling motion of the spacecraft along its bore sight coupled with inter- and intra-pixel sensitivity variations. We used a method similar to that described by Vanderburg & Johnson (2014) to reduce this systematic flux variation. Our light curve production pipeline is as follows. We first downloaded the target pixel files from MAST. We laid circular apertures around the brightest pixel within the "postage stamp" (the set of pixels of the *Kepler* photometer corresponding to a given source). To obtain the centroid position of the image, we fitted a 2-D Gaussian function to the in-aperture flux distribution. We then fitted a piecewise linear function between the flux variation and the centroid motion of target. The fitted piecewise linear function was then detrended from the observed flux variation.

2.3. *Transit search*

Before searching the light curve for transits, we first removed any long-term systematic or instrumental flux variations by fitting a cubic spline to the reduced light curve from the previous section. To look for periodic

[1] https://archive.stsci.edu/k2/

transit signals, we employed the Box-Least-Squares algorithm (BLS, Kovács et al. 2002). We improved the efficiency of the original BLS algorithm by using a non-linear frequency grid that takes into account the scaling of transit duration with orbital period (Ofir 2014). We also adopted the signal detection efficiency (SDE, Ofir 2014) which quantifies the significance of a detection. SDE is defined by the amplitude of peak in the BLS spectrum normalized by the local standard deviation. We empirically set a threshold of SDE > 6.5 for the balance between completeness and false alarm rate. In order to identify all the transiting planets in the same system, we progressively re-ran BLS after removing the transit signal detected in the previous iteration.

To search for additional transit signals which may have been missed by the transit search method described above, we used two separate pipelines: one based on the DST code (Cabrera et al. 2012), and one based on the wavelet-based filter routines `VARLET` and `PHALET` (Grziwa & Pätzold 2016). This helps to ensure higher detection rates, and the number of false positives is potentially reduced by utilizing multiple diagnostics. The DST code is optimized for space-based photometry and has been successfully applied to data from CoRoT and Kepler; we ran it on the light curves extracted by Vanderburg & Johnson (2014), which are publicly available from MAST. In the wavelet-based search we first used `VARLET` to remove long-term stellar variability in the light curves, and then searched for transits using a modified version of the BLS algorithm. Detected transit-like signals were then removed using `PHALET`, which combines phase-folding and a wavelet basis to approximate periodic features. In similar fashion to the above approach, we iterate this process of feature detection and removal to enable the detection of multi-planet systems.

2.4. *Candidate vetting*

We performed a quick initial vetting to identify obvious false positives among the transiting signals identified in the previous section. Planetary candidates that survived the various tests were followed up with speckle imaging and reconnaissance spectra for proper statistical validation. We tested for the presence of any "odd-even" variations and significant secondary eclipse, both of which are likely signatures of eclipsing binaries. The odd-even effect is the variation of the eclipse depth between the primary and secondary eclipse of an eclipsing binary. If mistaken for planetary transits, the primary and secondary eclipses will be the odd and even numbered transits.

We fitted Mandel & Agol (2002) model to the odd and even transits separately. If a systems shows odd-even variations with more than 3σ significance, it is flagged as a false positive. We also looked for any secondary eclipse in the light curve, using the Mandel & Agol (2002) model fit of the transits as a template for the occultation. After fitting the primary transits, we searched for secondary eclipses via an additional MCMC fitting step. We set the limb-darkening coefficients to zero and fixed all transit parameters except for two: the time of secondary eclipse and the depth of the eclipse. The resulting posterior distributions of these two parameters were then used to quantify the significance and phase of any putative secondary eclipses. For non-detections, we use the 3σ upper limit derived from the eclipse depth posterior to set the "maximum allowed secondary eclipse" constraint in our `vespa` analyses. If a system shows a secondary eclipse with more than 3σ significance, we calculated the geometric albedo using the depth of secondary eclipse. The object is likely self-luminous, hence likely a false positive, if the albedo is much greater than 1.

2.5. *Stellar rotation periods*

We also measured stellar rotation periods $P_{\rm rot}$ from the variability in the light curves induced by starspot modulation. About half of the light curves of our candidates exhibited a lack of rotational modulation, or the *K2* C10 time baseline was not long enough to constrain the period. For the rest, we used the autocorrelation function (ACF; e.g. McQuillan et al. 2014) to measure the rotational period, and we include these results in Table 1 along with initial estimates of the basic transit parameters of each candidate. To help ensure the validity of these measurements, we also used the Lomb-Scargle periodogram (Lomb 1976; Scargle 1982) to measure the rotational periods, and the results were in good agreement.

Table 1. Candidate planets detected in *K2* C10. *Kp* denotes magnitude in the *Kepler* bandpass.

EPIC	Kp [mag]	$P_{\rm orb}$ [days]	T_0 [BKJD]	T_{14} [hours]	Depth	SDE	$P_{\rm rot}$ [days]
201092629	11.9	26.810	2751.22	4.1	0.00090	13.2	22^{+6}_{-2}
201102594	15.6	6.514	2753.24	2.0	0.00624	8.2	25±3
201110617	12.9	0.813	2750.14	1.3	0.00029	16.2	16.8±2.5
201111557	11.4	2.302	2750.17	1.9	0.02268	7.6	12.0±1.8
201127519	11.6	6.179	2752.55	2.5	0.01303	11.6	—
201128338	13.1	32.655	2775.62	4.0	0.00159	6.7	15.6±2.2
201132684	11.7	10.061	2757.49	3.8	0.00070	8.7	13.8±1.3
201132684	11.7	5.906	2750.82	5.0	0.00015	9.7	13.8±1.3
201164625	11.9	2.711	2750.15	3.1	0.00020	6.7	12.5±1.5
201166680	10.9	24.941	2751.51	5.2	0.00019	6.6	—
201166680	10.9	11.540	2760.22	3.7	0.00016	7.8	—
201180665	13.1	17.773	2753.50	2.9	0.03662	11.2	—

Table 1 continued

Table 1 *(continued)*

EPIC	Kp [mag]	$P_{\rm orb}$ [days]	T_0 [BKJD]	T_{14} [hours]	Depth	SDE	$P_{\rm rot}$ [days]
201211526	11.7	21.070	2755.48	3.9	0.00030	8.3	—
201225286	11.7	12.420	2753.52	3.3	0.00065	11.6	20.8±1.6
201274010	13.9	13.008	2756.51	2.2	0.00065	7.7	—
201352100	12.8	13.383	2761.79	2.2	0.00120	12.5	36±11
201357643	12.0	11.893	2754.55	4.2	0.00107	12.3	—
201386739	14.4	5.767	2750.70	3.4	0.00134	11.1	35±6
201390048	12.0	9.455	2750.92	3.0	0.02669	7.7	—
201390927	14.2	2.638	2750.34	1.7	0.00110	12.9	—
201392505	13.4	27.463	2759.08	5.5	0.00150	9.3	—
201437844	9.2	21.057	2757.07	4.4	0.00100	10.0	—
201437844	9.2	9.560	2753.52	3.5	0.00030	9.8	—
201595106	11.7	0.877	2750.05	1.0	0.00025	9.4	—
201598502	14.3	7.515	2755.43	2.3	0.00129	7.5	—
201615463	12.0	8.527	2753.77	3.7	0.00016	7.2	—
228707509	14.8	15.351	2752.51	3.6	0.02386	13.6	—
228720681	13.8	15.782	2753.42	3.4	0.01028	14.3	9.8±1.1
228721452	11.3	4.563	2749.98	2.8	0.00020	12.6	—
228721452	11.3	0.506	2750.56	0.9	0.00010	9.6	—
228724899	13.3	5.203	2753.45	1.4	0.00113	12.3	—
228725791	14.3	6.492	2755.15	1.7	0.00110	9.8	32±3
228725791	14.3	2.251	2749.97	1.2	0.00100	7.3	32±3
228725972	12.5	4.477	2752.69	2.4	0.03270	11.5	—
228725972	12.5	10.096	2755.41	3.6	0.05928	13.0	—
228729473	11.5	16.773	2752.76	12.4	0.00199	11.6	36^{+5}_{-3}
228732031	11.9	0.369	2749.93	1.0	0.00040	15.1	9.4±1.9
228734900	11.5	15.872	2754.37	4.6	0.00034	8.0	—
228735255	12.5	6.569	2755.29	3.3	0.01280	12.6	31.1±2.0
228736155	12.0	3.271	2751.02	2.4	0.00027	9.3	—
228739306	13.3	7.172	2755.11	2.8	0.00070	8.1	—
228748383	12.5	12.409	2750.04	5.9	0.00024	8.0	—
228748826	13.9	4.014	2751.13	2.4	0.00102	13.2	39^{+6}_{-8}
228753871	13.2	18.693	2757.74	2.2	0.00082	7.7	16.4±2.3
228758778	14.8	9.301	2756.07	2.7	0.00214	7.8	—
228758948	12.9	12.203	2753.83	4.0	0.00128	12.4	11.3±1.7
228763938	12.6	13.814	2763.19	3.6	0.00036	8.8	—
228784812	12.6	4.189	2751.02	2.2	0.00014	8.9	—
228798746	12.7	2.697	2750.20	1.5	0.02587	14.1	—
228801451	11.0	8.325	2753.35	2.5	0.05325	12.9	19.5±2.7
228801451	11.0	0.584	2750.46	1.5	0.01625	10.0	19.5±2.7
228804845	12.6	2.860	2749.60	2.6	0.00020	7.3	—
228809391	12.6	19.580	2763.80	2.6	0.00100	8.3	—
228809550	14.7	4.002	2751.00	2.1	0.01259	12.5	—
228834632	14.9	11.730	2758.63	2.1	0.00111	8.6	23.6±2.1
228836835	14.9	0.728	2750.26	0.8	0.00068	15.4	—
228846243	14.5	25.554	2756.93	5.4	0.00220	10.5	—
228849382	13.8	12.120	2757.61	2.4	0.00120	7.6	—
228849382	13.8	4.097	2749.96	1.6	0.00052	8.8	—
228888935	14.1	5.691	2751.67	3.3	0.00533	10.3	7.2±1.1
228894622	13.3	1.964	2750.31	1.1	0.00183	16.3	20.8±2.4
228934525	13.4	3.676	2752.05	1.7	0.00110	14.2	28.3±3.1
228934525	13.4	7.955	2751.34	2.1	0.00110	11.4	28.3±3.1
228964773	14.9	37.209	2776.76	3.1	0.00280	6.9	—
228968232	14.7	5.520	2753.52	3.6	0.00097	8.6	—
228974324	12.9	1.606	2750.29	1.3	0.00034	13.1	22.0±2.3
228974907	9.3	20.782	2759.64	5.0	0.00010	7.2	—
229004835	10.2	16.138	2764.63	2.1	0.00036	10.6	22.2±2.5
229017395	13.2	19.099	2753.28	6.0	0.00049	8.1	—
229103251	13.7	11.667	2756.72	3.1	0.00114	9.9	—
229131722	12.5	15.480	2752.71	4.2	0.00037	8.3	—
229133720	11.5	4.037	2750.96	1.5	0.00091	12.4	11.8±1.3

2.6. *Transit modeling*

We used the orbital period, mid-transit time, transit depth, and transit duration identified by BLS as the starting points for more detailed transit modeling. The transit light curve was generated by the `Python` package `batman` (Kreidberg 2015). To reduce the data volume, we only use the light curve in a $3\times T_{14}$ window centered on the mid-transit times. We first tested if any of the systems showed strong transit timing variations (TTVs). We used the Python interface to the Levenberg-Marquardt non-linear least squares algorithm `lmfit` (Newville et al. 2014) to find the best-fit model of the phase-folded transit, and then fit this template to each transit separately to identify individual transit times of each candidate. Since none of the system presented in this work showed significant TTVs within the *K2* C10 observations, we assumed linear ephemerides in subsequent analyses.

The transit parameters in our linear ephemeris model include the orbital period $P_{\rm orb}$, the mid-transit time T_0, the planet-to-star radius ratio $R_p/R_\star$, the scaled orbital distance $a/R_\star$, the impact parameter $b \equiv a\cos i/R_\star$, and the transformed quadratic limb-darkening coefficients q_1 and q_2. Instead of fixing the parameters of the quadratic limb-darkening law to theoretical values based on stellar models, in this work we opt to allow these parameters to vary, as this allows for error propagation from stellar uncertainties. We utilize the available stellar parameters and their uncertainties to impose Gaussian priors on the limb-darkening coefficients (i.e. in the non-transformed parameter space, u_1 and u_2). To determine the location and width of these priors, we used a Monte Carlo method to sample the stellar parameters of each candidate host star ($T_{\rm eff}$, $\log g$, and [Fe/H]), and then used these to derive distributions of u_1 and u_2 from an interpolated grid based on the limb-darkening coefficients for the Kepler bandpass tabulated by Claret et al. (2012). We used the median and standard deviation of these distributions to define the Gaussian limb-darkening priors, and used uniform priors for all other parameters. Depending on the uncertainty in the stellar parameters, the limb-darkening priors determined in this way have typical widths of ∼10%, which is comparable to the uncertainty in the models used to predict them (e.g. Csizmadia et al. 2013; Müller et al. 2013). In addition, when the stars are active we do not expect agreement between theoretical and observed limb darkening because the tabulated theoretical values do not take into account the effects of stellar spots and faculae (Csizmadia et al. 2013). To account for the 30 min integration time of long cadence *K2* photometry, we used the built-in feature of `batman` to super-sample the model light curve

by a factor of 16 before averaging every 3 min window (Kipping 2010).

We adopted a Gaussian likelihood function, and found the maximum likelihood solution using `scipy.optimize` (Jones et al. 2001–present). We then sampled the joint posterior distribution using `emcee` (Foreman-Mackey et al. 2013), a Python implementation of the affine-invariant Markov Chain Monte Carlo ensemble sampler (Goodman & Weare 2010). We assumed the errors to be Gaussian, independent, and identically distributed, and thus described by a single parameter. In the maximum likelihood fits, we fixed the value of this parameter to the standard deviation of the out of transit flux, and during MCMC we fit for this value as a free parameter. We launched 100 walkers in the vicinity of the maximum likelihood solution and ran the sampler for 5000 steps, discarding the first 1000 as "burn-in." To ensure that the resultant marginalized posterior distributions consisted of 1000's of independent samples (enough for negligible sampling error) we computed the autocorrelation time of each parameter, and visual inspection revealed the posteriors to be smooth and unimodal. We summarize the transit parameter posterior distributions in Table 5 using the 16^{th}, 50^{th}, and 84^{th} percentiles, and we use the posterior samples to compute other quantities of interest throughout this work (i.e. R_p, $T_{\rm eq}$). The phase-folded light curves of the candidates are shown in Figure 1, with best-fitting transit model and 1σ (68%) credible region over-plotted.

3. SPECKLE IMAGING

We observed candidate host stars with the NASA Exoplanet Star and Speckle Imager (NESSI) on the 3.5-m WIYN telescope at the Kitt Peak National Observatory. NESSI is a new instrument that uses high-speed electron-multiplying CCDs (EMCCDs) to capture sequences of 40 ms exposures simultaneously in two bands (Scott et al. (2016), Scott et al., in prep.). Data were collected following the procedures described by Howell et al. (2011). We conducted all observations in two bands simultaneously: a 'blue' band centered at 562nm with a width of 44nm, and a 'red' band centered at 832nm with a width of 40nm. The pixel scales of the 'blue' and 'red' EMCCDs are 0.0175649″ and 0.0181887″ per pixel, respectively. We make all of our speckle imaging data publicly available via the community portal ExoFOP[2]. We list the individual NESSI data products used in this work in Table 9.

Speckle imaging data were reduced following the procedures described by Howell et al. (2011), resulting in diffraction limited 4.6″ × 4.6″ reconstructed images (256 × 256 pixels) of each target star. The methodology has been described in detail in previous works (e.g. Horch et al. 2009, 2012, 2017), but we provide a brief review here for convenience.

First, the autocorrelation function of each 40 ms exposure is summed and Fourier transformed, resulting in the average spatial frequency power spectrum. The speckle transfer function is then deconvolved by dividing the target's power spectrum by that of the corresponding point source calibrator, yielding the square of the modulus estimate of the target's Fourier transform. The phase information can then be recovered from bispectral analysis, as first described by Lohmann et al. (1983). This is accomplished by computing the Fourier transform of the summed triple correlation function of the exposures, which in combination with the modulus estimate yields the complex Fourier transform of the target. This is then filtered with a low-pass 2-d Gaussian before being inverse transformed, yielding the reconstructed image.

We extract background sensitivity limits from the reconstructed images by computing the mean and standard deviation of a series of concentric annuli centered on the target star, as described by Howell et al. (2011). We then compute contrast curves by fitting a cubic spline to the kernel-smoothed 5σ sensitivity limits, expressed as a magnitude difference relative to the target star as a function of radius. For stars of moderate brightness ($V = 10 - 12$ mag) we typically achieve contrasts of ~ 4 magnitudes at 0.2″. See Figure 2 for a plot showing all of the contrast curves obtained in this work. We detect 4 candidate host stars with secondaries, see Table 2.

Table 2. Stars with detected companions. All detections made in the 832nm band.

EPIC	Δarcsec	Δmag	θ [deg. E of N]	Note
201352100	0.387	3.37	312.054	a
201390927	0.883	1.14	341.286	a
201392505	0.242	3.68	42.491	b
228964773	0.332	2.08	43.499	b

Note—a: The quadrant of the position angle is ambiguous, meaning it could be off by exactly 180 degrees. b: The binary model fit is of poor quality, so uncertainty may be larger than typical.

4. HIGH RESOLUTION SPECTROSCOPY

4.1. *McDonald/Tull*

Most of the high resolution spectra presented in this paper were obtained with the Tull Coudé cross-dispersed

[2] https://exofop.ipac.caltech.edu

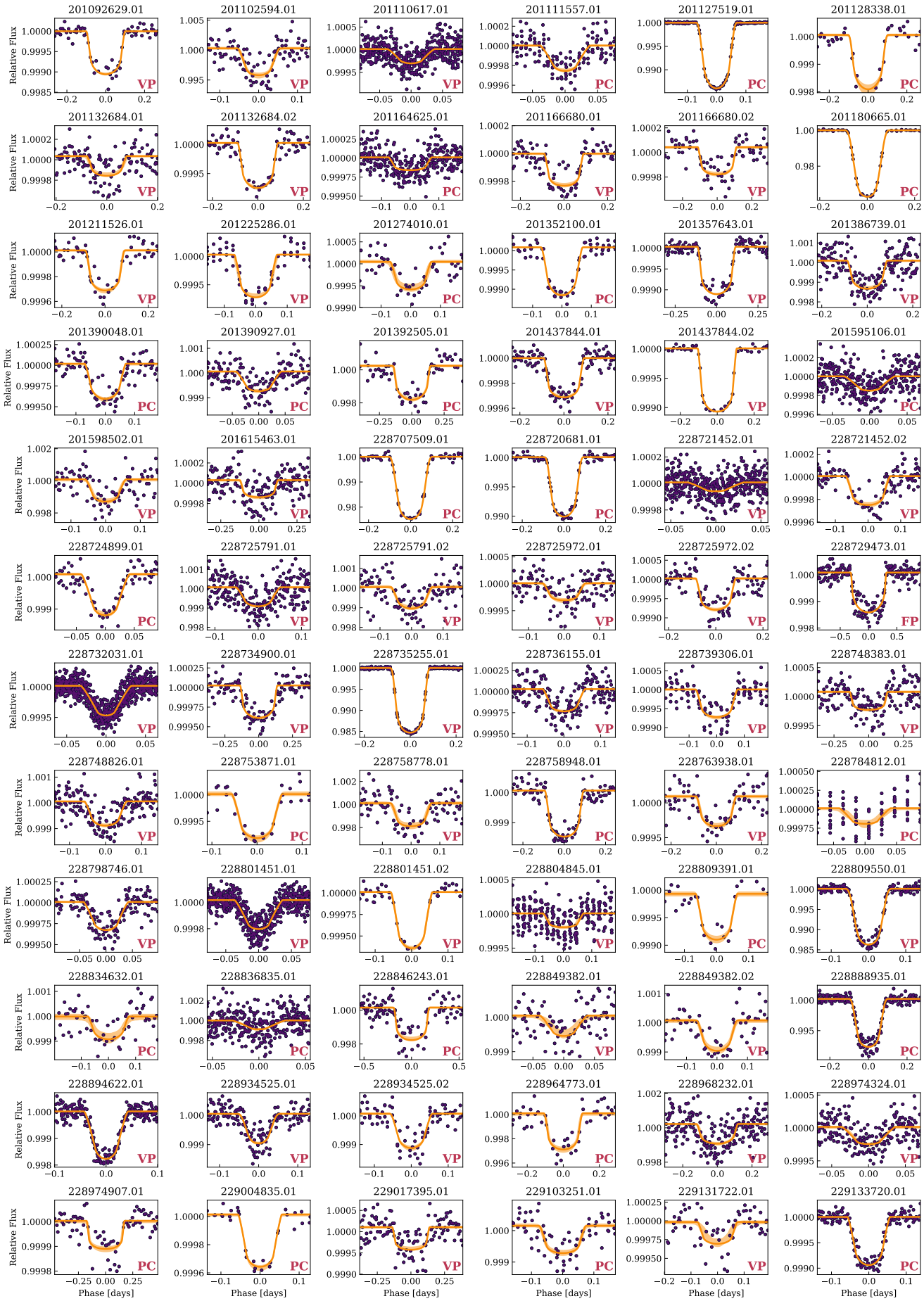

Figure 1. Phase-folded transits (purple), with the best-fit transit model and 1σ credible region overplotted (orange). Candidate dispositions are displayed in the lower-right corners (see Section 5).

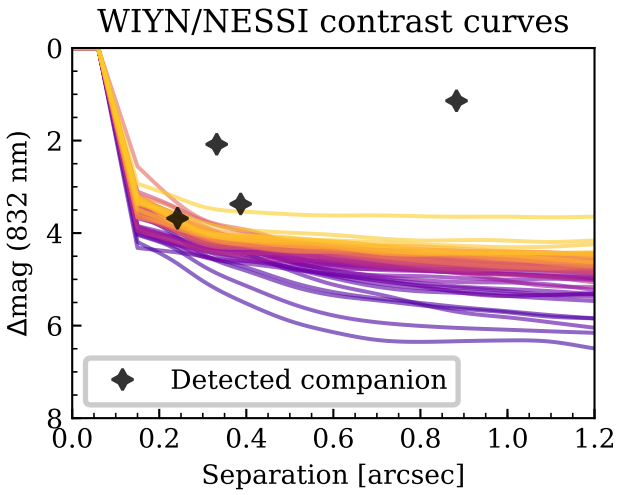

Figure 2. Contrast curves and detected companions

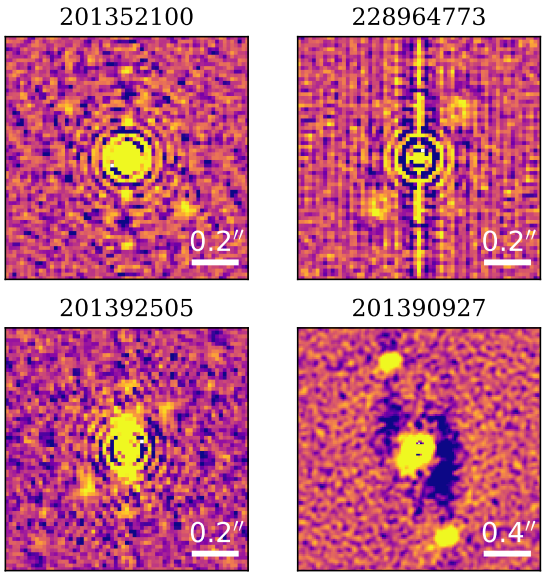

Figure 3. Reconstructed 832nm images of stars with detected companions.

echelle spectrograph (Tull et al. 1995) at the Harlan J. Smith 2.7m telescope at McDonald Observatory. Observations were conducted with the 1.2×8.2″ slit, yielding a resolving power of $R \sim 60,000$. The spectra cover 375-1020 nm, with increasingly larger inter-order gaps longward of 570 nm. For each target star, we obtained three successive short exposures in order to allow removal of energetic particle hits on the CCD detector. We used an exposure meter to obtain an accurate flux-weighted barycentric correction and to give an exposure length that resulted in a signal/noise ratio of about 30 per pixel. Bracketing exposures of a Th-Ar hollow cathode lamp were obtained in order to generate a wavelength calibration and to remove spectrograph drifts. This enabled calculation of absolute radial velocities from the spectra. The raw data were processed using IRAF routines to remove the bias level, inter-order scattered light, and pixel-to-pixel ("flat field") CCD sensitivity variations. We traced the apertures for each spectral order and used an optimal extraction algorithm to obtain the detected stellar flux as a function of wavelength.

We computed stellar parameters from our reconnaissance Tull spectra using *Kea* (Endl & Cochran 2016). In brief, we used standard IRAF routines to perform flat fielding, bias subtraction, and order extraction, and we used a blaze function determined from high SNR flat field exposures to correct for curvature induced by the blaze. *Kea* uses a large grid of synthetic model stellar spectra to compute stellar effective temperatures, surface gravities, and metallicities. See Table 6 for the stellar parameters used in this work. From a comparison with higher SNR spectra obtained with Keck/HIRES we found typical uncertainties of 100 K in $T_{\rm eff}$, 0.12 dex in [Fe/H], and 0.18 dex in $\log g$. For a detailed description of Kea see Endl & Cochran (2016).

4.2. *NOT/FIES*

We also used the FIbre-fed Échelle Spectrograph (FIES; Frandsen & Lindberg 1999; Telting et al. 2014) on the 2.56-m Nordic Optical Telescope (NOT) of Roque de los Muchachos Observatory (La Palma, Spain) to collect high-resolution ($R \approx 67\,000$) spectra of four C10 candidate host stars: 228729473, 228735255 (K2-140; Giles et al. (2018), Korth et al., submitted to MNRAS), 201127519, and 228732031 (K2-131; Dai et al. 2017). The observations were carried out between February 15 to May 23, 2017 UTC, within observing programs 54-027, 55-019, and 55-202. We followed the same strategy as in Gandolfi et al. (2013) and traced the RV drift of the instrument by bracketing the science exposures with 90-sec ThAr spectra. We reduced the data using standard IRAF routines and extracted the RVs via multi-order cross-correlations using different RV standard stars observed with the same instrument.

4.3. *TNG/HARPS-N*

We observed the stars 228801451, 228732031 (K2-131; Dai et al. 2017), 201595106, and 201437844 (HD 106315; Crossfield et al. 2017; Rodriguez et al. 2017) with the HARPS-N spectrograph ($R \approx 115000$; Cosentino et al. 2012) mounted at the 3.58 m Telescopio Nazionale Galileo (TNG) of Roque de los Muchachos Observatory (La Palma, Spain). The observations were performed in January 2017 as part of observing programs

A34TAC_10 and A34TAC_44. We reduced the data using the dedicated off-line pipeline and extracted the RVs by cross-correlating the échelle spectra with a G2 numerical mask. The HARPS-N data of 228732031 have been published by our team in Dai et al. (2017). We refer the reader to that paper for a detailed description and analysis of the data. We list the results of our analysis of these spectra in Table 10.

4.4. *Stellar properties*

We obtained spectra for 27 candidate host stars in this work, from which we derived $T_{\rm eff}$, $\log g$, [Fe/H], and $v \sin i$, as described in Section 4.1. We augment this set of spectroscopic stellar parameters with values from the literature for an additional 14 candidate host stars (Rodriguez et al. 2017; Hirano et al. 2018a; Mayo et al. 2018). To maximize both the quality and uniformity of the final set of stellar parameters we use in this work, we adopted the following strategy. First, we gathered 2MASS JHK photometry and Gaia DR2 parallaxes for all stars; 2MASS photometry is available in the EPIC, and we cross-matched to Gaia DR2 using both position and optical magnitude agreement (Kp and Gaia G band). We then used the `isochrones` (Morton 2015a) interface to the Dartmouth stellar model grid (Dotter et al. 2008) to estimate stellar parameters and their uncertainties using the `MultiNest` sampling algorithm (Feroz et al. 2013). For those stars with parameters from spectroscopic analyses, we imposed Gaussian priors on $T_{\rm eff}$, $\log g$, and [Fe/H], with mean and standard deviation set by the spectroscopically derived values and their uncertainties. We also ran the same analysis without including parallax, as a check on the quality of the parameters derived in this manner without any distance information; unsurprisingly, we found that including parallax yielded the biggest improvement for stars lacking spectroscopy. This is perhaps most important for the M dwarfs in our sample, which suffer from systematically underestimated radii in the EPIC (see e.g. Dressing et al. 2017).

As an additional quality check, we also performed spectral analyses for the targets 201127519, 201437844, 201595106, and 228801451, using spectra from FIES and HARPS-N and `SpecMatch-emp` (Yee et al. 2017). `SpecMatch-emp` fits the input spectra to hundreds of library template spectra collected by the California Planet Search, and the stellar parameters ($T_{\rm eff}$, $R_\star$, and [Fe/H]) are estimated based on the interpolation of the parameters for best-matched library stars. Among them 201127519, 201595106, and 228801451 were also observed with the Tull spectrograph, and the resulting parameters by `SpecMatch-emp` are in agreement within $\sim 1.5\sigma$ with those estimated from the Tull spectra by the *Kea* code. For HD 106315, we obtained $T_{\rm eff} = 6326 \pm 110$ K, $R_\star = 1.86 \pm 0.30$ $R_\odot$, and [Fe/H] $= -0.20 \pm 0.08$. While $T_{\rm eff}$ and [Fe/H] agrees within 1σ with the literature values (Rodriguez et al. 2017; Crossfield et al. 2017), $R_\star$ exhibits a moderate disagreement with that in the literature ($R_\star = 1.281^{+0.051}_{-0.058}$ $R_\odot$ Rodriguez et al. 2017). This is probably due to the small number of library stars in `SpecMatch-emp` in the region with $T_{\rm eff} > 6300$ K, but this disagreement does not have any impact on our results.

5. PLANET VALIDATION

5.1. *Statistical framework*

We use the open source `vespa` software package (Morton 2012, 2015b) to compute the false positive probabilities (FPPs) of each planet candidate. `vespa` uses the `TRILEGAL` Galaxy model (Girardi et al. 2005) to compute the posterior probabilities of both planetary and non-planetary scenarios given the observational constraints, and considers false positive scenarios involving simple eclipsing binaries, blended background eclipsing binaries, and hierarchical triple systems. `vespa` models the physical properties of the host star, taking into account any available broadband photometry and spectroscopic stellar parameters, and compares a large number of simulated scenarios to the observed phase-folded light curve. Both the size of the photometric aperture and contrast curve constraints are accounted for in the calculations, as well as any other observational constraints such as the maximum depth of secondary eclipses allowed by the data. We adopt a fiducial validation criterion of FPP < 0.01, which is reasonably conservative and also consistent with the literature (e.g. Montet et al. 2015; Crossfield et al. 2016; Morton et al. 2016). `vespa` utilizes the contrast curves derived from the observations listed in Table 9 and described in Section 3. To minimize the possibility of errors in the `vespa` calculations induced by zero-point offsets or underestimated uncertainties in broadband photometry, we opt to use only the well-calibrated 2MASS JHK magnitudes and their uncertainties, taken from the EPIC, in addition to the *Kepler* band magnitude required by `vespa`. The stellar parameters used as input to `vespa` are identical to those used in our uniform `isochrones` analysis (see Section 4.4). In addition to stellar parameters, `vespa` utilizes basic system properties (i.e. RA, Dec, $P_{\rm orb}$, $R_p/R_\star$), as well as contrast curves (see Section 3) and constraints on secondary eclipse depth and maximum exclusion radii (see Table 8). We tabulate candidate parameters along with their FPPs and final dispositions in Table 5, and the full `vespa` likelihoods are listed in

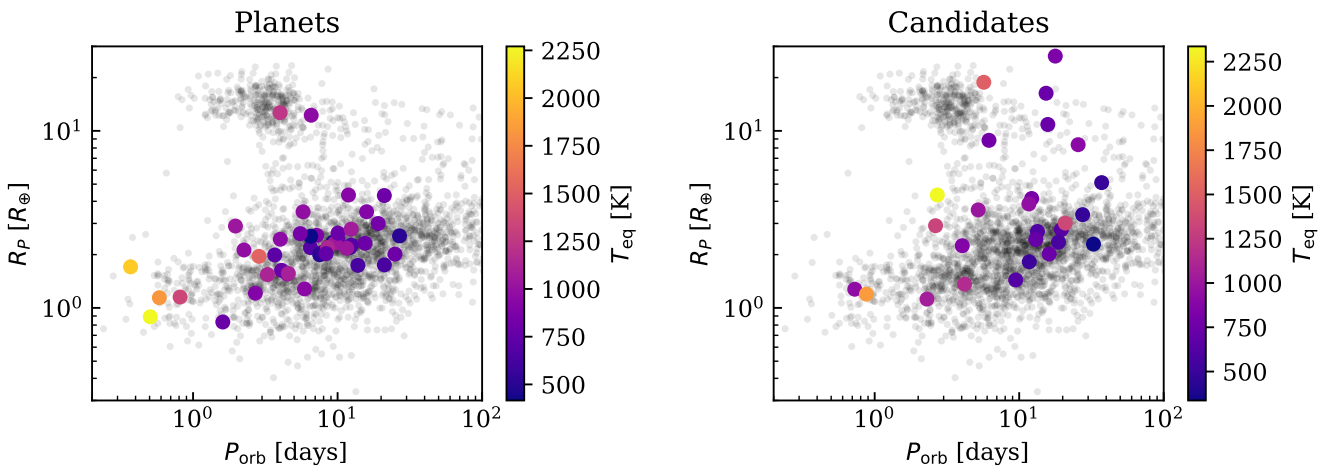

Figure 4. Validated (left) and candidate (right) planets from C10 against the background of previously confirmed or validated planets, colored by their equilibrium temperature (assuming a Bond albedo of 0.3).

Table 7. We denote final dispositions as follows: "VP" = validated planet; "PC" = planet candidate; "FP" = false positive.

All of the candidates we detect in multi-planet systems meet the fiducial validation criterion of FPP < 1%. However, FPPs computed with `vespa` treat only the individual planet candidates in isolation, and thus do not take into account any multiplicity in each system. Stars with multiple transiting planet candidates have been shown to exhibit a lower false positive rate by an order of magnitude (Lissauer et al. 2011, 2012, 2014). For this reason we apply a "multiplicity boost" factor to the planet probability appropriate for each candidate in a multi-planet system. Lissauer et al. (2012) estimated a multiplicity boost factor of 25 for systems containing 2 planet candidates in the *Kepler* field, and we apply the same factor in this work. To check that this factor is appropriate for *K2* C10, we follow Sinukoff et al. (2016) and utilize equations (2) and (4) of Lissauer et al. (2012) to estimate the sample purity P from the integrated FPP of our sample and the number of planet candidates we detect (72). This estimate of P is quite high, perhaps due to a lack of contamination from background stars due to the high galactic latitude of the field, or due to our team's vetting procedures. The fraction of detected planet candidates in multi-systems (18/72) in conjunction with the high sample purity yields a multiplicity boost which is significantly higher than the factor of 25 estimated by Lissauer et al. (2012) for the *Kepler* field. Although the true value is likely to be higher, we conservatively apply only a factor of 25, consistent with Lissauer et al. (2012), and the FPPs in Table 5 reflect this accordingly.

5.2. *Stellar companions*

To ensure that the FPPs computed by `vespa` are reliable, we take into account the presence of any nearby stars detected in speckle or archival imaging. Table 2 lists the nearby stars we detected via speckle imagine, along with their separations and delta-magnitudes relative to the primary stars. Figure 3 shows the reconstructed speckle images for these stars, and Figure 2 shows these detections relative to the ensemble of contrast curves from all of our speckle images. Table 3 lists those stars found in the EPIC to be near and bright enough to be the source of the observed transit signals.

5.2.1. *Companions detected in high resolution imaging*

On the nights of 2017-03-15, 2017-03-17, and 2017-03-18 we acquired speckle imaging of the stars 201352100, 201390927, 201392505, and 228964773 (see Table 9). We detected companions in the reconstructed images (see Figure 3), so we assessed the possibility that the transit signal might not originate from the primary stars. We used the following relation between the observed transit depth δ' and the true transit depth δ in the presence of dilution from a companion Δm magnitudes fainter than the primary star:

$$\delta' = \frac{\delta}{1 + 10^{0.4\Delta m}} \quad (1)$$

Assuming a maximum eclipse depth of 100% (i.e. a brown dwarf — M dwarf binary) we can potentially rule out the secondary star as the source of the observed signal. For shallower transits the maximum allowed dilution from the primary is larger, and therefore even a relatively faint secondary source cannot be ruled out as

Table 3. EPIC sources within the photometric apertures which are bright enough to produce the observed transit-like signals.

EPIC	Contaminant	ρ [arcsec]	ΔKp [mag]
201111557	201111694	15.90	5.187
201164625	201164669	17.58	3.228
201595106	201595004	13.62	5.839
228707509	228707572	12.48	1.563
228720681	228720649	7.86	2.905
228758948	228758983	9.00	3.267

the host. For each of these four of these candidates, the secondary source is bright enough (given the observed transit depth) that we cannot rule out the possibility they are the source of the signal (see Table 2). For this reason, we do not validate any of these candidates as planets, as we do not know the true source of the signal (and therefore the true planet size), even though they all have low FPPs.

5.2.2. *Companions in the EPIC*

In addition to analyzing the scenarios involving companions detected in high resolution speckle imaging, we also performed a search of the EPIC for any additional stars within the photometric apertures which could be the source of the observed signals. Most of these queries yielded no stars within the aperture other than the primary, but there were some cases in which the query yielded a star bright enough to be the source of the observed transit signal; we list these cases in Table 3. Despite their low FPPs, we do not validate these candidates because we do not know which star is the true host. As we expect most of these candidates to be genuine planets, they present good validation opportunities via higher angular resolution follow-up transit observations, either from the ground or from space (i.e. with *Spitzer* or *CHEOPS*).

5.2.3. *Archival imaging*

As a check on the accuracy of the sources comprising the EPIC, we also queried 1'×1' Pan-STARRS-1[3] *grizy* images centered at the position of each candidate host star. We found good agreement with the catalog query: nearby stars found by the catalog query were clearly visible in the images, and no nearby bright sources were seen in the images that were not previously found by the catalog query. We show these images in Figure 5, with overplotted circular regions illustrating the size and location of the apertures used to extract photometry from the *K2* pixel data.

[3] Data release 1, dated December 19, 2016, available at http://ps1images.stsci.edu/cgi-bin/ps1cutouts

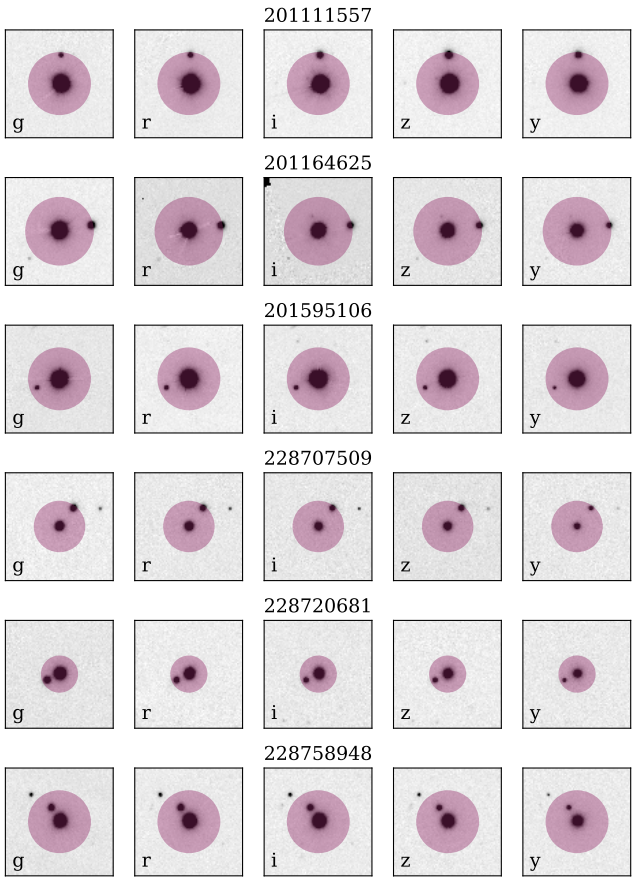

Figure 5. Archival *grizy* imaging from Pan-STARRS-1. Shown here are candidate planet hosts with nearby bright stars within the *K2* apertures (represented by circular shaded regions). Assuming a maximum eclipse depth of 100%, the observed transit-like signal could potentially be reproduced by scenarios in which the signal is actually a faint eclipsing binary diluted by the flux from the brighter primary star. We note, however, that such scenarios would sometimes result in more "V-shaped" transits than what we observe.

5.3. *Multi-aperture light curve analysis*

In light of several recent cases of contamination from false positives in statistically validated planet samples (Shporer et al. 2017; Cabrera et al. 2017), we also scrutinized our candidates at the pixel level. To do so, we extracted light curves from different sized apertures and looked for signs of a dependence of transit depth on aperture radius. In some cases, these light curves are too noisy to draw conclusions from, as they are extracted

from "non-optimal" apertures. However, this analysis is especially important when there are widely separated neighboring stars (i.e. several *Kepler* pixels away) that still contribute flux to the *K2* apertures, in which case it may be possible to determine the origin of the transit-like signal by this method. Based on these analyses we found that the transit signal associated with the candidate 201164625.01 most likely originates from the neighboring star, 201164669 (see Table 3 and Figure 5). We also detected suspicious transit depth behavior in the light curves of 201392505.01 and 228964773.01, both of which have nearby companions detected in speckle imaging. Intriguingly, these companions are well within a *Kepler* pixel of the target star, so even the smallest aperture possible (one *Kepler* pixel) should contain light from both the primary and secondary stars. This result may indicate the presence of another (undetected) star further away, and suggests that such multi-aperture analyses should be useful for ranking the quality of candidates when high resolution imaging is unavailable.

5.4. *Transit SNR*

As a final step in the validation process, we compute the transit SNR for each candidate in order to enforce a minimum transit quality standard for all planets in the validated sample. We compute the transit SNR using the simple approximation that the signal scales with the transit depth and the square root of the number of transits (e.g. Bouma et al. 2017). We estimate the noise by computing the standard deviation of the out-of-transit photometry used in our light curve fits and scaling it from the *K2* observing cadence to the transit duration of each candidate. We find median SNR values of 17.1 and 17.6 for the validated and candidate samples, respectively. The slightly lower SNR of the validated sample is likely attributable to the fact that candidates with higher FPPs are typically larger and have correspondingly deeper transits, whereas the vast majority of our validated planets are sub-Neptunes (see Figure 4). Our validated sample consists of planets with SNR $>$ 10, with the exception of K2-254 b and K2-247 c, which have SNR values of 6.7 and 8.9, respectively. However, these are both in multi-planet systems, which increases our confidence in the veracity of the transit signals. We argue that candidates with relatively low SNR found in systems with multiple validated candidates need not be regarded with as much suspicion as similarly low SNR candidates in single-candidate systems; this is related to, but more qualitative than, the "multi-boost" argument of Lissauer et al. (2012). Indeed, many interesting planets with low SNR likely remain to be found in both the *Kepler* and *K2* data (e.g. Shallue & Vanderburg 2018).

5.5. *Pipeline comparison*

To check the quality of our light curves and provide an additional layer of confidence in our candidates, we performed a parallel analysis using light curves from an independent *K2* pipeline. We first downloaded the light curves of Vanderburg & Johnson (2014) from MAST for all the targets listed in Table 1, then detrended the light curves by fitting a second order polynomial to the out-of-transit data using `exotrending` (Barragán & Gandolfi 2017). To explore the transit model parameter space with MCMC, we used `pyaneti` (Barragán et al. 2017a) to fit the detrended light curves with uniform priors for all parameters; more description of the `pyaneti` MCMC evolution and parameter estimation can be found in Barragán et al. (2017b) and Gandolfi et al. (2017). For the majority of candidates, the main transit parameters of interest ($P_{\rm orb}$, $R_p/R_\star$, b, and $a/R_\star$) are consistent within 1σ between our two independent analyses, although there are some cases in which marginally significant differences were found. These differences are likely to be the result of different handling of the *K2* systematics and/or the stellar variability in the light curves. The overall good agreement between these two independently-derived sets of transit parameters provides an additional layer of confidence in the quality of the candidates. The results of this comparison are listed in Table 12.

6. DISCUSSION

6.1. *Validated planets*

We validate 44 planets out of our sample of 72 candidates, and tabulate the FPPs along with parameter estimates of interest in Table 5. Of the 44 validated planets we report here, 20 of them have been previously statistically validated or confirmed: 201598502.01, 228934525.01, and 228934525.02 (K2-153 b, K2-154 bc; Hirano et al. 2018a); 228735255.01 (K2-140 b; Giles et al. (2018), Korth et al., submitted to MNRAS); 201437844.01 and 201437844.02 (HD 106315 bc; Crossfield et al. 2017; Rodriguez et al. 2017); 228732031.01 (K2-131 b; Dai et al. 2017); and 13 others were recently validated by Mayo et al. (2018). In the left panel of Figure 4 we plot the planetary radii, orbital periods, and equilibrium temperatures of the validated planets in the sample.

We investigated the impact of these new planets to the population of currently known planets by querying the NASA Exoplanet Archive[4] (Akeson et al. 2013). We computed the fractional enhancement to the known pop-

[4] https://exoplanetarchive.ipac.caltech.edu/

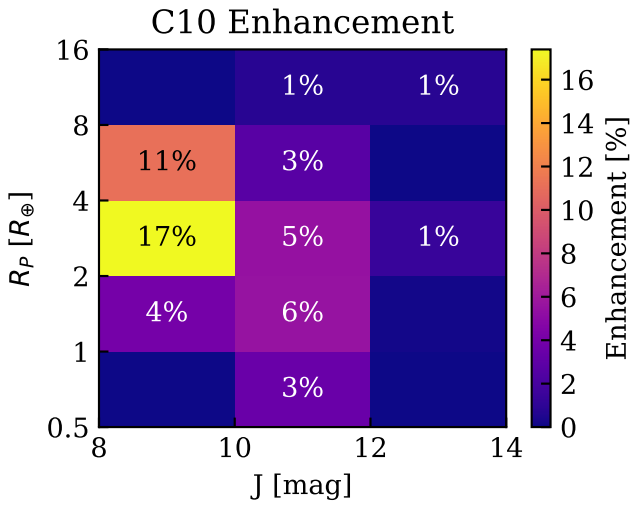

Figure 6. The fractional enhancement to the population of previously validated or confirmed planets from our sample of 44 validated C10 planets.

ulation due to the 44 planets as a function of planet size and host star brightness (see Figure 6). As of June 12, 2018, the populations of super-Earths ($R_p \approx 1$–$2R_\oplus$), sub-Neptunes ($R_p \approx 2$–$4R_\oplus$), and sub-Saturns ($R_p \approx 4$–$8R_\oplus$) orbiting bright stars ($J = 8$–10 mag) are enhanced by ∼4%, ∼17%, and ∼11%, respectively. Because of the brightness of the host stars, many of these planets are ideal for detailed characterization studies via precision Doppler and transmission spectroscopy, which we discuss in greater detail in Section 6.4.

6.2. *Candidates*

Out of the 72 planet candidates we present here, 27 are not validated. Most cannot be validated due to the FPP being above our fiducial validation criterion of 1% or the presence of a contaminating star within the photometric aperture. See Table 7 for the likelihoods of various false positive scenarios and the planet scenario, as computed by `vespa`. There are several candidates which we do not validate for other reasons, which we discuss below. In the right panel of Figure 4 we plot the planetary radii, orbital periods, and equilibrium temperatures of the non-validated candidates.

The candidate 228729473.01 exhibits a long transit duration, and subsequent spectroscopic analyses revealed large RV variations which are consistent with the candidate being a false positive involving an M dwarf eclipsing a sub-giant, see Csizmadia et al (in prep.) for more details. The light curve of 229133720.01 exhibits low levels of variability in phase with the transit signal, which could be due to ellipsoidal variations; thus we do not validate the candidate in spite of its low FPP. Although 201390048.01 was recently validated (K2-162 b; Mayo et al. 2018), we found marginal evidence of odd-even variations in the light curve of this candidate, which could be an indication that the signal is actually caused by an eclipsing binary at twice the estimated orbital period. Although `vespa` accounts for this scenario in its FPP calculation, we do not validate the candidate even though its FPP is below 1%. The candidate 201180665.01 has a relatively high FPP (∼64%), and also a suspiciously large radius estimate (∼26 $R_\oplus$). Although spectroscopic characterization could yield a different radius estimate for the host star (and thus also for the candidate), we conclude that this is most likely an eclipsing M dwarf companion. The candidates 228974907.01, and 228846243.01 do not have particularly low FPPs, but they may be interesting targets for further observations due to their relatively long orbital periods. The candidate 201128338.01 was statistically validated previously in the literature (K2-152 b; Hirano et al. 2018a); we find a similarly low FPP, but we do not validate it simply because it has fewer than three transits in the *K2* photometry (and thus odd/even variations in transit depth cannot be robustly ruled out). Further observations will shed light on the true nature of these candidates, either by measuring RV variations with precision spectrographs or via simultaneous multi-band transit observations with instruments such as MuSCAT (Narita et al. 2015) and MuSCAT2 (a *griz* clone of MuSCAT now in operation at Teide Observatory).

The integrated FPP is ∼2.1 for the full set of 72 candidates, which implies the existence of two false positives in the sample. We have already confirmed that 228729473.01 is a false positive via RV observations (see Csizmadia et al., in prep.), and we suspect 229133720.01, 201390048.01, and 201180665.01 of being false positives, as described above. Therefore, we expect no false positives among the remainder of the sample, and most of the 27 unvalidated candidates could be statistically validated or confirmed by future observations.

6.3. *Interesting new systems*

6.3.1. *Ultra-short period planets*

Ultra-short period planets (USPs) are defined by having orbital periods less than one day (e.g. Sanchis-Ojeda et al. 2013, 2015). Our validated planet sample contains four USPs: K2-131 b (Dai et al. 2017); K2-156 b and K2-223 b (Mayo et al. 2018); and K2-229 b (Mayo et al. 2018; Santerne et al. 2018). These planets join a growing list of USPs discovered by *K2* (e.g. Vanderburg et al. 2016c; Christiansen et al. 2017; Gandolfi et al. 2017; Adams et al. 2017; Dai et al. 2017; Barragán et al.

2017b; Malavolta et al. 2018). The radii of these USPs place all three of them below the recently observed gap in the radius distribution (Fulton et al. 2017; Van Eylen et al. 2017) which was predicted as a consequence of photoevaporation (e.g. Owen & Wu 2013; Lopez & Fortney 2014). These three USPs are therefore likely to be rocky and have high densities, consistent with having lost any primordial or secondary atmospheres they might once have had. Of these validated USPs, we measured the metallicity of the host stars spectroscopically for three of them; K2-229 appears to have only a modestly sub-solar metallicity of -0.09 ± 0.02 [Fe/H], but K2-131 and K2-156 have more significantly sub-solar metallicities of -0.17 ± 0.03 and -0.25 ± 0.06 [Fe/H], respectively (see Table 6). Due to their small size, these USPs are likely to have a mass less than 5–6 $M_\oplus$, and thus the sub-solar metallicity of their host stars would be consistent with the USP mass-metallicity trend noted by Sinukoff et al. (2017) (i.e. similar to Kepler-78 b and Kepler-10 b).

The G dwarf K2-223 and K dwarf K2-229 are both relatively bright ($Kp \sim 11$ mag), and host planets with predicted masses and Doppler semi-amplitudes well within the reach of current precision spectrographs, such as HARPS or HIRES. K2-156 b orbits a slightly fainter star and has a slightly smaller predicted mass and Doppler semi-amplitude, but is also a viable target for characterization with today's instrumentation. Such mass measurements would yield densities and constrain the bulk compositions of these USPs, which would enable tests of USP formation theories.

In addition to the four validated USPs mentioned above, we also note that our sample contains two USP candidates: 201595106.01 and 228836835.01. We do not validate 201595106.01 because of the presence of a faint star in the EPIC with a ΔKp of 5.839 and a separation of 13.62″(see Table 3), which is within the photometric aperture we used to extract the *K2* light curve. We do not validate 228836835.01 because it has a FPP of ∼4% and thus does not meet our validation criterion. Future observations could potentially rule out false positive scenarios for both of these candidates, resulting in the validation of two more USPs from *K2* C10.

6.3.2. *Multi-planet systems*

Of the 44 validated planets in our sample, 18 of them were found in two-planet systems, which enables the study of their orbital architectures and evolution. Four of these systems have orbital architectures with period ratios just wide of a 2:1 commensurability, and two are close to a 3:1 commensurability. The pairs closest to 2:1 are K2-243 bc and K2-154 bc, which both have $P_c/P_b \approx 2.16$. The relatively large fraction of multi-planet systems (4/9) in our sample with period ratios just wide of a 2:1 commensurability is reminiscent of the distribution of orbital architectures observed with *Kepler* (Fabrycky et al. 2014). K2-254 bc and K2-247 bc are both just inside a 3:1 commensurability, with period ratios of $P_c/P_b \approx 2.96$ and $P_c/P_b \approx 2.89$, respectively. Although we did not detect any significant TTVs in the *K2* data, some of these systems may have TTVs which could be detected with higher cadence transit observations.

Intriguingly, two of the four validated USPs in the sample were found in two-planet systems with large period ratios, similar to the Kepler-10 system: K2-223 bc has $P_c/P_b \approx 9.02$, and K2-229 bc has $P_c/P_b \approx 14.25$. The presence of an additional transiting planet decreases the likelihood that these USPs reached their current orbits via dynamical scattering, as this would increase the chances of higher mutual inclinations; even after tidal circularization, the geometric transit probability would be decreased by a higher likelihood of non-coplanarity. This is consistent with previous analyses in which USP systems have been noted to be dynamically cold (e.g. Dai et al. 2017).

6.4. *Characterization targets*

We predicted the masses of the candidates using the probabilistic mass-radius relation of Wolfgang et al. (2016)[5] (see Table 5). The predicted masses enabled us to compute other quantities of interest, which we then used to identify potentially interesting targets for follow-up characterization via Doppler and transmission spectroscopy.

6.4.1. *Doppler targets*

We computed the expected Doppler semi-amplitude due to the reflex motion of the host star induced by each planet (see Table 5). We used these expected semi-amplitudes in conjunction with the brightness of the host stars to identify planets in the sample which are good targets for radial velocity (RV) follow-up study using current and future facilities. Such RV observations will reveal the planets' densities and constrain their bulk compositions. This is of particular interest for relatively small planets with radii in the range $1.5 - 2.5\ R_\oplus$ because such measurements could enable tests of planet formation theories and post-processes, such as the photoevaporation (e.g. Owen & Wu 2013; Lopez & Fortney 2014), which has been proposed to explain the observed gap in the radius distribution (Fulton et al. 2017; Van Eylen et al. 2017). However, because of the difficulty of

[5] https://github.com/dawolfgang/MRrelation

detecting the small Doppler signals of such planets, it is especially important to identify such planets which are orbiting relatively bright stars, for which the RV precision required to measure their masses is more readily obtainable. Table 4 lists validated planets with predicted Doppler semi-amplitudes greater than 1 $\mathrm{m\,s^{-1}}$ orbiting stars brighter than $Kp = 12$ mag. For convenience, we also list planetary orbital periods and stellar rotational periods (when available); potentially confounding quasi-periodic RV signals produced by stellar magnetic activity are less likely to present a challenge for mass measurement when the orbital period is far from the stellar rotational period (or a harmonic). We note that 228732031.01 (K2-131 b) and 228801451.01 (K2-229 b) both already have measured masses via precision RVs (Dai et al. 2017; Santerne et al. 2018).

Another possibly interesting RV target is K2-257 b, a sub-Earth-size planet orbiting a nearby M dwarf. Although the planet's radius is only $0.83^{+0.06}_{-0.05}$ $R_\oplus$, the Doppler semi-amplitude could be as high as $\sim$1 $\mathrm{m\,s^{-1}}$ due to the low mass of the host star and the planet's short orbital period. The host star is moderately bright ($Kp = 12.873$, $J = 10.477$ mag), so this presents an opportunity to directly measure the mass of a sub-Earth with one of today's high precision optical or NIR spectrographs. Such a measurement would yield the planet's density and constrain its composition, as well as improve our knowledge of the mass-radius relation for small planets. The only other sub-Earth-size planet known to transit a similarly bright M dwarf is Kepler-138 b, for which the mass has been measured only via transit timing variations (Jontof-Hutter et al. 2015; Almenara et al. 2018).

6.4.2. *Atmospheric targets*

In order to identify viable new targets for atmospheric studies via transmission spectroscopy, we used the properties of the host stars and planets to predict atmospheric scale heights and the amplitudes of the wavelength dependence of transit depth (δ_{TS}). Following Miller-Ricci et al. (2009), we calculated the atmospheric scale height H and δ_{TS} for each validated planet by

$$H = \frac{29.26}{(\mu/28.96)} \frac{T_{\mathrm{eq}}}{g} \quad [\mathrm{m}] \tag{2}$$

$$\delta_{\mathrm{TS}} \sim 10\, H \cdot R_p / R_\star^2, \tag{3}$$

where μ, T_{eq}, and g are the mean molecular weight, planet equilibrium temperature, and planet surface gravity, respectively. We used the predicted planet mass estimated in Section 6.4 to predict the surface gravity, and assumed a bond albedo of 0.3 and a mean molecular weight $\mu = 2$ (hydrogen-dominated atmosphere) for each planet (see Table 11). We note that this assumption for μ is likely to be invalid for the smaller planets in our sample (i.e. $R_p \lesssim 1.5$–2 $R_\oplus$), as they are not likely to have substantial hydrogen-dominated atmospheres; these smaller planets likely have higher mean molecular weight atmospheres, which would make their characterization via transmission spectroscopy more challenging. The validated planets K2-140 b and K2-255 b both orbit relatively bright host stars ($J < 12$ mag) and have large expected transmission spectroscopy signals ($\delta_{\mathrm{TS}} > 200$ ppm), and thus could be interesting targets for future atmospheric characterization.

Table 4. Validated planets with predicted Doppler semi-amplitudes greater than 1 $\mathrm{m\,s^{-1}}$ orbiting stars brighter than $Kp = 12$ mag. Note: 228721452.01 is not listed here because it doesn't meet these criteria, but RV measurements to constrain the mass of 228721452.02 could also reveal the inner planet's mass, as both Keplerian signals would need to be accounted for in the RV analysis.

EPIC	Kp [mag]	K_{pred} [$\mathrm{m\,s^{-1}}$]	R_p [$R_\oplus$]	P_{orb} [days]	P_{rot} [days]
201092629.01	11.858	$2.5^{+0.7}_{-0.7}$	2.55	26.8199	22^{+6}_{-2}
201132684.01	11.678	$1.3^{+0.7}_{-0.7}$	1.28	5.9028	13.8±1.3
201132684.02	11.678	$3.0^{+0.8}_{-0.8}$	2.64	10.0605	13.8±1.3
201166680.01	10.897	$1.8^{+0.6}_{-0.6}$	2.17	11.5418	—
201166680.02	10.897	$1.2^{+0.5}_{-0.4}$	2.01	24.9460	—
201211526.01	11.696	$1.5^{+0.6}_{-0.6}$	1.75	21.0688	—
201225286.01	11.729	$2.3^{+0.7}_{-0.7}$	2.26	12.4220	20.8±1.6
201357643.01	11.998	$5.7^{+1.2}_{-1.1}$	4.34	11.8931	—
201437844.01	9.234	$2.3^{+0.7}_{-0.7}$	2.32	9.5580	—
201437844.02	9.234	$3.9^{+0.8}_{-0.7}$	4.31	21.0579	—
201615463.01	11.964	$2.1^{+0.7}_{-0.7}$	2.19	8.5270	—
228721452.02	11.325	$1.8^{+0.9}_{-0.8}$	1.57	4.5633	—
228732031.01	11.937	$5.3^{+2.3}_{-2.2}$	1.70	0.3693	9.4±1.9
228734900.01	11.535	$2.9^{+0.7}_{-0.6}$	3.49	15.8721	—
228801451.01	10.955	$2.2^{+1.0}_{-1.2}$	1.14	0.5843	19.5±2.7
228801451.02	10.955	$2.3^{+0.8}_{-0.8}$	2.03	8.3273	19.5±2.7

7. SUMMARY

We detected 72 planet candidates in *K2* Campaign 10 and obtained high resolution imaging and spectroscopy follow-up observations to characterize the host stars. We performed detailed modeling of the light curves and used the resulting transit parameters to compute physical planet properties. We used the planet and host star properties to predict masses and atmospheric signals, which enabled us to identify good targets for future characterization via Doppler and transmission spectroscopy. We statistically validated 44 planets, leaving a remainder of 27 candidates and one false positive. We expect nearly all of these remaining candidates to be real plan-

ets, which could potentially be validated via further observations and analysis.

This work was carried out as part of the KESPRINT consortium. The WIYN/NESSI observations were conducted as part of an approved NOAO observing program (P.I. Livingston, proposal ID 2017A-0377). Data presented herein were obtained at the WIYN Observatory from telescope time allocated to NN-EXPLORE through the scientific partnership of the National Aeronautics and Space Administration, the National Science Foundation, and the National Optical Astronomy Observatory. This work was supported by a NASA WIYN PI Data Award, administered by the NASA Exoplanet Science Institute. NESSI was funded by the NASA Exoplanet Exploration Program and the NASA Ames Research Center. NESSI was built at the Ames Research Center by Steve B. Howell, Nic Scott, Elliott P. Horch, and Emmett Quigley. The authors are honored to be permitted to conduct observations on Iolkam Du'ag (Kitt Peak), a mountain within the Tohono O'odham Nation with particular significance to the Tohono O'odham people. J. H. L. gratefully acknowledges the support of the Japan Society for the Promotion of Science (JSPS) Research Fellowship for Young Scientists. This work was supported by Japan Society for Promotion of Science (JSPS) KAKENHI Grant Number JP16K17660. M.E. and W.D.C. were supported by NASA grant NNX16AJ11G to The University of Texas. This paper includes data collected by the *Kepler* mission. Funding for the *Kepler* mission is provided by the NASA Science Mission directorate.

Facilities: Kepler, WIYN (NESSI), McDonald (Tull), NOT (FIES), TNG (HARPS-N)

Software: `scipy`, `emcee`, `batman`, `vespa`, `IRAF`, `pyaneti`, `exotrending`

REFERENCES

Adams, E. R., Jackson, B., Endl, M., et al. 2017, AJ, 153, 82

Akeson, R. L., Chen, X., Ciardi, D., et al. 2013, PASP, 125, 989

Almenara, J. M., Díaz, R. F., Dorn, C., Bonfils, X., & Udry, S. 2018, MNRAS, 478, 460

Barragán, O., & Gandolfi, D. 2017, Exotrending: Fast and easy-to-use light curve detrending software for exoplanets, Astrophysics Source Code Library, , , ascl:1706.001

Barragán, O., Gandolfi, D., & Antoniciello, G. 2017a, pyaneti: Multi-planet radial velocity and transit fitting, Astrophysics Source Code Library, , , ascl:1707.003

Barragán, O., Gandolfi, D., Dai, F., et al. 2017b, ArXiv e-prints, arXiv:1711.02097

Bouma, L. G., Winn, J. N., Kosiarek, J., & McCullough, P. R. 2017, ArXiv e-prints, arXiv:1705.08891

Cabrera, J., Csizmadia, S., Erikson, A., Rauer, H., & Kirste, S. 2012, A&A, 548, A44

Cabrera, J., Barros, S. C. C., Armstrong, D., et al. 2017, A&A, 606, A75

Christiansen, J. L., Vanderburg, A., Burt, J., et al. 2017, AJ, 154, 122

Ciardi, D. R., Crossfield, I. J. M., Feinstein, A. D., et al. 2018, AJ, 155, 10

Claret, A., Hauschildt, P. H., & Witte, S. 2012, VizieR Online Data Catalog, 354

Cosentino, R., Lovis, C., Pepe, F., et al. 2012, in Proc. SPIE, Vol. 8446, Ground-based and Airborne Instrumentation for Astronomy IV, 84461V

Crossfield, I. J. M., Petigura, E., Schlieder, J. E., et al. 2015, ApJ, 804, 10

Crossfield, I. J. M., Ciardi, D. R., Petigura, E. A., et al. 2016, ApJS, 226, 7

Crossfield, I. J. M., Ciardi, D. R., Isaacson, H., et al. 2017, AJ, 153, 255

Csizmadia, S., Pasternacki, T., Dreyer, C., et al. 2013, A&A, 549, A9

Dai, F., Winn, J. N., Gandolfi, D., et al. 2017, AJ, 154, 226

David, T. J., Hillenbrand, L. A., Petigura, E. A., et al. 2016a, Nature, 534, 658

David, T. J., Conroy, K. E., Hillenbrand, L. A., et al. 2016b, AJ, 151, 112

Dotter, A., Chaboyer, B., Jevremović, D., et al. 2008, ApJS, 178, 89

Dressing, C. D., Vanderburg, A., Schlieder, J. E., et al. 2017, AJ, 154, 207

Endl, M., & Cochran, W. D. 2016, PASP, 128, 094502

Fabrycky, D. C., Lissauer, J. J., Ragozzine, D., et al. 2014, ApJ, 790, 146

Feroz, F., Hobson, M. P., Cameron, E., & Pettitt, A. N. 2013, ArXiv e-prints, arXiv:1306.2144

Foreman-Mackey, D., Hogg, D. W., Lang, D., & Goodman, J. 2013, PASP, 125, 306

Frandsen, S., & Lindberg, B. 1999, in Astrophysics with the NOT, ed. H. Karttunen & V. Piirola, 71

Fridlund, M., Gaidos, E., Barragán, O., et al. 2017, A&A, 604, A16
Fulton, B. J., Petigura, E. A., Howard, A. W., et al. 2017, AJ, 154, 109
Gaidos, E., Mann, A. W., Rizzuto, A., et al. 2017, MNRAS, 464, 850
Gandolfi, D., Parviainen, H., Fridlund, M., et al. 2013, A&A, 557, A74
Gandolfi, D., Barragán, O., Hatzes, A. P., et al. 2017, AJ, 154, 123
Giles, H. A. C., Bayliss, D., Espinoza, N., et al. 2018, MNRAS, 475, 1809
Girardi, L., Groenewegen, M. A. T., Hatziminaoglou, E., & da Costa, L. 2005, A&A, 436, 895
Goodman, J., & Weare, J. 2010, Communications in Applied Mathematics and Computational Science, Vol. 5, No. 1, p. 65-80, 2010, 5, 65
Grziwa, S., & Pätzold, M. 2016, ArXiv e-prints, arXiv:1607.08417
Guenther, E. W., Barragán, O., Dai, F., et al. 2017, A&A, 608, A93
Hirano, T., Dai, F., Gandolfi, D., et al. 2018a, AJ, 155, 127
Hirano, T., Dai, F., Livingston, J. H., et al. 2018b, AJ, 155, 124
Horch, E. P., Howell, S. B., Everett, M. E., & Ciardi, D. R. 2012, AJ, 144, 165
Horch, E. P., Veillette, D. R., Baena Gallé, R., et al. 2009, AJ, 137, 5057
Horch, E. P., Casetti-Dinescu, D. I., Camarata, M. A., et al. 2017, AJ, 153, 212
Howell, S. B., Everett, M. E., Sherry, W., Horch, E., & Ciardi, D. R. 2011, AJ, 142, 19
Howell, S. B., Sobeck, C., Haas, M., et al. 2014, PASP, 126, 398
Jones, E., Oliphant, T., Peterson, P., et al. 2001–present, SciPy: Open source scientific tools for Python, ,
Jontof-Hutter, D., Rowe, J. F., Lissauer, J. J., Fabrycky, D. C., & Ford, E. B. 2015, Nature, 522, 321
Kipping, D. M. 2010, MNRAS, 408, 1758
Kovács, G., Zucker, S., & Mazeh, T. 2002, A&A, 391, 369
Kreidberg, L. 2015, PASP, 127, 1161
Lissauer, J. J., Ragozzine, D., Fabrycky, D. C., et al. 2011, ApJS, 197, 8
Lissauer, J. J., Marcy, G. W., Rowe, J. F., et al. 2012, ApJ, 750, 112
Lissauer, J. J., Marcy, G. W., Bryson, S. T., et al. 2014, ApJ, 784, 44
Livingston, J. H., Dai, F., Hirano, T., et al. 2018, AJ, 155, 115
Lohmann, A. W., Weigelt, G., & Wirnitzer, B. 1983, ApOpt, 22, 4028
Lomb, N. R. 1976, Ap&SS, 39, 447
Lopez, E. D., & Fortney, J. J. 2014, ApJ, 792, 1
Malavolta, L., Mayo, A. W., Louden, T., et al. 2018, ArXiv e-prints, arXiv:1801.03502
Mandel, K., & Agol, E. 2002, ApJL, 580, L171
Mann, A. W., Gaidos, E., Mace, G. N., et al. 2016a, ApJ, 818, 46
Mann, A. W., Newton, E. R., Rizzuto, A. C., et al. 2016b, AJ, 152, 61
Mann, A. W., Gaidos, E., Vanderburg, A., et al. 2017, AJ, 153, 64
Mayo, A. W., Vanderburg, A., Latham, D. W., et al. 2018, AJ, 155, 136
McQuillan, A., Mazeh, T., & Aigrain, S. 2014, ApJS, 211, 24
Miller-Ricci, E., Seager, S., & Sasselov, D. 2009, ApJ, 690, 1056
Montet, B. T., Morton, T. D., Foreman-Mackey, D., et al. 2015, ApJ, 809, 25
Morton, T. D. 2012, ApJ, 761, 6
—. 2015a, isochrones: Stellar model grid package, Astrophysics Source Code Library, , , ascl:1503.010
—. 2015b, VESPA: False positive probabilities calculator, Astrophysics Source Code Library, , , ascl:1503.011
Morton, T. D., Bryson, S. T., Coughlin, J. L., et al. 2016, ApJ, 822, 86
Müller, H. M., Huber, K. F., Czesla, S., Wolter, U., & Schmitt, J. H. M. M. 2013, A&A, 560, A112
Narita, N., Fukui, A., Kusakabe, N., et al. 2015, Journal of Astronomical Telescopes, Instruments, and Systems, 1, 045001
Newville, M., Stensitzki, T., Allen, D. B., & Ingargiola, A. 2014, LMFIT: Non-Linear Least-Square Minimization and Curve-Fitting for Python¶, , , doi:10.5281/zenodo.11813
Niraula, P., Redfield, S., Dai, F., et al. 2017, AJ, 154, 266
Obermeier, C., Henning, T., Schlieder, J. E., et al. 2016, AJ, 152, 223
Ofir, A. 2014, A&A, 561, A138
Owen, J. E., & Wu, Y. 2013, ApJ, 775, 105
Pepper, J., Gillen, E., Parviainen, H., et al. 2017, AJ, 153, 177
Petigura, E. A., Schlieder, J. E., Crossfield, I. J. M., et al. 2015, ApJ, 811, 102
Rodriguez, J. E., Zhou, G., Vanderburg, A., et al. 2017, AJ, 153, 256
Sanchis-Ojeda, R., Rappaport, S., Winn, J. N., et al. 2013, ApJ, 774, 54

Sanchis-Ojeda, R., Rappaport, S., Pallè, E., et al. 2015, ApJ, 812, 112
Santerne, A., Brugger, B., Armstrong, D. J., et al. 2018, Nature Astronomy, 2, 393
Scargle, J. D. 1982, ApJ, 263, 835
Scott, N. J., Howell, S. B., & Horch, E. P. 2016, in Proc. SPIE, Vol. 9907, Optical and Infrared Interferometry and Imaging V, 99072R
Shallue, C. J., & Vanderburg, A. 2018, AJ, 155, 94
Shporer, A., Zhou, G., Vanderburg, A., et al. 2017, ApJL, 847, L18
Sinukoff, E., Howard, A. W., Petigura, E. A., et al. 2016, ApJ, 827, 78
—. 2017, AJ, 153, 271
Smith, A. M. S., Cabrera, J., Csizmadia, S., et al. 2018, MNRAS, 474, 5523
Telting, J. H., Avila, G., Buchhave, L., et al. 2014, Astronomische Nachrichten, 335, 41
Tull, R. G., MacQueen, P. J., Sneden, C., & Lambert, D. L. 1995, PASP, 107, 251
Van Eylen, V., Agentoft, C., Lundkvist, M. S., et al. 2017, ArXiv e-prints, arXiv:1710.05398
Van Eylen, V., Dai, F., Mathur, S., et al. 2018, MNRAS, arXiv:1805.01860
Vanderburg, A., & Johnson, J. A. 2014, PASP, 126, 948
Vanderburg, A., Montet, B. T., Johnson, J. A., et al. 2015, ApJ, 800, 59
Vanderburg, A., Becker, J. C., Kristiansen, M. H., et al. 2016a, ApJL, 827, L10
Vanderburg, A., Latham, D. W., Buchhave, L. A., et al. 2016b, ApJS, 222, 14
Vanderburg, A., Bieryla, A., Duev, D. A., et al. 2016c, ApJL, 829, L9
Wolfgang, A., Rogers, L. A., & Ford, E. B. 2016, ApJ, 825, 19
Yee, S. W., Petigura, E. A., & von Braun, K. 2017, ApJ, 836, 77

Table 5. Planet and candidate parameters.

EPIC	Name	$P_{\rm orb}$ [days]	T_0 [BKJD]	a [$R_\star$]	b	R_p [$R_\star$]	a [AU]	R_p [$R_\oplus$]	$T_{\rm eq}$ [K]	M_P [$M_\oplus$]	$K_{\rm pred}$ [m s^{-1}]	$\rho_{\star,LC}$ [$\rho_\odot$]	FPP	Disposition
201092629.01	K2-241 b	$26.81990^{+0.00245}_{-0.00247}$	$2751.2063^{+0.0035}_{-0.0034}$	$43.3^{+3.8}_{-9.9}$	$0.41^{+0.30}_{-0.28}$	$0.0312^{+0.0023}_{-0.0012}$	$0.1567^{+0.0007}_{-0.0008}$	$2.55^{+0.18}_{-0.10}$	507^{+5}_{-5}	$9.1^{+2.4}_{-2.4}$	$2.4^{+0.7}_{-0.7}$	$1.5^{+0.4}_{-0.8}$	7×10^{-8}	VP
201102594.01	K2-242 b	$6.51389^{+0.00082}_{-0.00083}$	$2753.2400^{+0.0054}_{-0.0054}$	$22.1^{+3.8}_{-5.6}$	$0.42^{+0.32}_{-0.29}$	$0.0633^{+0.0051}_{-0.0044}$	$0.0494^{+0.0004}_{-0.0004}$	$2.54^{+0.21}_{-0.19}$	416^{+8}_{-8}	$9.0^{+2.7}_{-2.5}$	$5.9^{+1.7}_{-1.6}$	$3.4^{+2.1}_{-2.0}$	6×10^{-12}	VP
201110617.01	K2-156 b	$0.81314^{+0.00007}_{-0.00008}$	$2750.1427^{+0.0041}_{-0.0038}$	$4.1^{+0.6}_{-0.9}$	$0.41^{+0.32}_{-0.27}$	$0.0161^{+0.0014}_{-0.0010}$	$0.0149^{+0.0001}_{-0.0001}$	$1.15^{+0.10}_{-0.07}$	1347^{+18}_{-19}	$2.7^{+1.5}_{-1.5}$	$2.4^{+1.3}_{-1.4}$	$1.4^{+0.7}_{-0.7}$	2×10^{-12}	VP
201111557.01		$2.30183^{+0.00028}_{-0.00030}$	$2750.1688^{+0.0052}_{-0.0052}$	$11.8^{+2.1}_{-3.0}$	$0.42^{+0.33}_{-0.28}$	$0.0144^{+0.0014}_{-0.0010}$	$0.0313^{+0.0003}_{-0.0004}$	$1.12^{+0.11}_{-0.08}$	1054^{+55}_{-55}	$2.4^{+1.6}_{-1.4}$	$1.4^{+0.9}_{-0.8}$	$4.1^{+2.6}_{-2.4}$	3×10^{-4}	PC
201127519.01		$6.17887^{+0.00007}_{-0.00007}$	$2752.5473^{+0.0005}_{-0.0005}$	$18.1^{+0.2}_{-0.6}$	$0.17^{+0.14}_{-0.11}$	$0.1058^{+0.0011}_{-0.0007}$	$0.0613^{+0.0007}_{-0.0007}$	$8.84^{+0.14}_{-0.13}$	772^{+10}_{-10}	$44.8^{+16.2}_{-12.1}$	$17.9^{+6.6}_{-4.8}$	$2.1^{+0.1}_{-0.2}$	4×10^{-2}	PC
201128338.01	K2-152 b	$32.64790^{+0.01141}_{-0.01483}$	$2775.6222^{+0.0135}_{-0.0073}$	$58.8^{+2.6}_{-2.9}$	$0.25^{+0.24}_{-0.17}$	$0.0344^{+0.0037}_{-0.0037}$	$0.1716^{+0.0012}_{-0.0012}$	$2.29^{+0.25}_{-0.24}$	337^{+3}_{-3}	$8.0^{+2.9}_{-2.7}$	$2.2^{+0.8}_{-0.7}$	$2.6^{+0.4}_{-0.4}$	1×10^{-7}	PC
201132684.01	K2-158 c	$5.90279^{+0.00191}_{-0.00233}$	$2750.8828^{+0.0131}_{-0.0120}$	$11.3^{+2.4}_{-2.9}$	$0.41^{+0.34}_{-0.28}$	$0.0123^{+0.0012}_{-0.0009}$	$0.0622^{+0.0006}_{-0.0006}$	$1.28^{+0.13}_{-0.10}$	948^{+13}_{-13}	$3.6^{+2.0}_{-1.9}$	$1.3^{+0.8}_{-0.7}$	$0.6^{+0.4}_{-0.3}$	3×10^{-8}	VP
201132684.02	K2-158 b	$10.06049^{+0.00134}_{-0.00148}$	$2757.4834^{+0.0080}_{-0.0064}$	$19.1^{+1.6}_{-4.0}$	$0.38^{+0.31}_{-0.27}$	$0.0255^{+0.0016}_{-0.0008}$	$0.0887^{+0.0008}_{-0.0008}$	$2.64^{+0.16}_{-0.10}$	794^{+11}_{-11}	$9.6^{+2.4}_{-2.5}$	$3.0^{+0.8}_{-0.8}$	$0.9^{+0.3}_{-0.5}$	8×10^{-8}	VP
201164625.01		$2.71189^{+0.00068}_{-0.00056}$	$2750.1362^{+0.0112}_{-0.0179}$	$5.5^{+1.1}_{-1.5}$	$0.43^{+0.35}_{-0.30}$	$0.0121^{+0.0010}_{-0.0008}$	$0.0461^{+0.0004}_{-0.0004}$	$4.34^{+0.43}_{-0.35}$	2336^{+59}_{-60}	$17.9^{+4.4}_{-3.8}$	$5.5^{+1.4}_{-1.2}$	$0.3^{+0.2}_{-0.2}$	4×10^{-3}	PC
201166680.01	K2-243 b	$11.54182^{+0.00272}_{-0.00221}$	$2760.2062^{+0.0079}_{-0.0102}$	$21.2^{+2.0}_{-4.5}$	$0.39^{+0.31}_{-0.27}$	$0.0144^{+0.0008}_{-0.0007}$	$0.1087^{+0.0014}_{-0.0014}$	$2.17^{+0.14}_{-0.12}$	1035^{+36}_{-35}	$7.4^{+2.4}_{-2.3}$	$1.8^{+0.6}_{-0.6}$	$1.0^{+0.3}_{-0.5}$	9×10^{-5}	VP
201166680.02	K2-243 c	$24.94598^{+0.00491}_{-0.00561}$	$2751.5050^{+0.0077}_{-0.0072}$	$35.6^{+4.0}_{-9.2}$	$0.40^{+0.34}_{-0.27}$	$0.0133^{+0.0009}_{-0.0009}$	$0.1817^{+0.0022}_{-0.0024}$	$2.01^{+0.15}_{-0.13}$	801^{+27}_{-28}	$6.7^{+2.4}_{-2.3}$	$1.2^{+0.4}_{-0.4}$	$1.0^{+0.4}_{-0.6}$	1×10^{-4}	VP
201180665.01		$17.77297^{+0.00009}_{-0.00009}$	$2753.4986^{+0.0002}_{-0.0002}$	$33.3^{+0.3}_{-0.3}$	$0.68^{+0.01}_{-0.01}$	$0.1892^{+0.0008}_{-0.0009}$	$0.1404^{+0.0029}_{-0.0030}$	$26.44^{+0.65}_{-0.65}$	830^{+34}_{-33}	$184.3^{+148.7}_{-79.4}$	$40.8^{+33.0}_{-17.6}$	$1.6^{+0.0}_{-0.0}$	6×10^{-1}	PC
201211526.01	K2-244 b	$21.06884^{+0.00320}_{-0.00325}$	$2755.4749^{+0.0062}_{-0.0065}$	$38.3^{+5.5}_{-10.1}$	$0.44^{+0.32}_{-0.30}$	$0.0174^{+0.0013}_{-0.0009}$	$0.1418^{+0.0010}_{-0.0011}$	$1.75^{+0.13}_{-0.10}$	638^{+7}_{-7}	$5.7^{+2.4}_{-2.3}$	$1.5^{+0.6}_{-0.6}$	$1.7^{+0.8}_{-1.0}$	7×10^{-4}	VP
201225286.01	K2-159 b	$12.42205^{+0.00180}_{-0.00182}$	$2753.5082^{+0.0074}_{-0.0077}$	$27.9^{+3.8}_{-6.9}$	$0.44^{+0.30}_{-0.30}$	$0.0250^{+0.0018}_{-0.0011}$	$0.1013^{+0.0008}_{-0.0009}$	$2.26^{+0.17}_{-0.11}$	684^{+8}_{-8}	$7.9^{+2.4}_{-2.5}$	$2.3^{+0.7}_{-0.7}$	$1.9^{+0.9}_{-1.1}$	2×10^{-4}	VP
201274010.01		$13.01130^{+0.00520}_{-0.00422}$	$2756.5150^{+0.0086}_{-0.0123}$	$26.7^{+5.8}_{-6.3}$	$0.42^{+0.31}_{-0.29}$	$0.0255^{+0.0025}_{-0.0024}$	$0.1062^{+0.0013}_{-0.0013}$	$2.43^{+0.25}_{-0.24}$	713^{+21}_{-21}	$8.5^{+2.5}_{-2.7}$	$2.4^{+0.7}_{-0.8}$	$1.5^{+1.2}_{-0.8}$	9×10^{-2}	PC
201352100.01		$13.38382^{+0.00116}_{-0.00114}$	$2761.7895^{+0.0032}_{-0.0033}$	$33.9^{+2.8}_{-7.0}$	$0.38^{+0.30}_{-0.27}$	$0.0326^{+0.0020}_{-0.0011}$	$0.1038^{+0.0007}_{-0.0006}$	$2.70^{+0.17}_{-0.10}$	608^{+9}_{-9}	$9.8^{+2.4}_{-2.5}$	$3.0^{+0.7}_{-0.8}$	$2.9^{+0.8}_{-1.5}$	2×10^{-3}	PC
201357643.01	K2-245 b	$11.89307^{+0.00065}_{-0.00063}$	$2754.5524^{+0.0018}_{-0.0018}$	$17.5^{+1.2}_{-3.1}$	$0.38^{+0.28}_{-0.26}$	$0.0317^{+0.0013}_{-0.0006}$	$0.0959^{+0.0006}_{-0.0006}$	$4.34^{+0.19}_{-0.14}$	923^{+14}_{-14}	$18.0^{+3.8}_{-3.4}$	$5.7^{+1.2}_{-1.1}$	$0.5^{+0.1}_{-0.2}$	2×10^{-4}	VP
201386739.01	K2-246 b	$5.76918^{+0.00081}_{-0.00082}$	$2750.6761^{+0.0064}_{-0.0062}$	$11.1^{+1.1}_{-2.3}$	$0.41^{+0.29}_{-0.27}$	$0.0341^{+0.0021}_{-0.0017}$	$0.0602^{+0.0004}_{-0.0004}$	$3.49^{+0.25}_{-0.21}$	977^{+19}_{-18}	$13.6^{+3.0}_{-2.8}$	$5.3^{+1.2}_{-1.1}$	$0.5^{+0.2}_{-0.3}$	6×10^{-5}	VP
201390048.01	K2-162 b	$9.45889^{+0.00104}_{-0.00107}$	$2750.9076^{+0.0047}_{-0.0042}$	$23.6^{+2.4}_{-5.0}$	$0.41^{+0.30}_{-0.29}$	$0.0190^{+0.0014}_{-0.0009}$	$0.0795^{+0.0006}_{-0.0006}$	$1.44^{+0.11}_{-0.07}$	631^{+8}_{-8}	$4.5^{+2.3}_{-2.2}$	$1.6^{+0.9}_{-0.8}$	$2.0^{+0.7}_{-1.0}$	2×10^{-3}	PC
201390927.01		$2.63800^{+0.00030}_{-0.00029}$	$2750.3409^{+0.0042}_{-0.0046}$	$10.9^{+1.6}_{-2.9}$	$0.42^{+0.33}_{-0.28}$	$0.0265^{+0.0025}_{-0.0019}$	$0.0370^{+0.0011}_{-0.0012}$	$2.91^{+0.40}_{-0.33}$	1313^{+90}_{-88}	$10.8^{+3.1}_{-2.9}$	$5.1^{+1.6}_{-1.4}$	$2.5^{+1.3}_{-1.5}$	3×10^{-5}	PC
201392505.01		$27.47083^{+0.01089}_{-0.01286}$	$2759.0795^{+0.0186}_{-0.0163}$	$30.9^{+3.3}_{-7.5}$	$0.40^{+0.33}_{-0.28}$	$0.0412^{+0.0032}_{-0.0021}$	$0.1657^{+0.0017}_{-0.0017}$	$3.36^{+0.26}_{-0.18}$	480^{+7}_{-7}	$13.0^{+3.0}_{-2.7}$	$3.2^{+0.7}_{-0.7}$	$0.5^{+0.2}_{-0.3}$	7×10^{-8}	PC
201437844.01	HD 106315 b	$9.55804^{+0.00165}_{-0.00170}$	$2753.5267^{+0.0067}_{-0.0068}$	$17.7^{+1.6}_{-4.4}$	$0.40^{+0.33}_{-0.28}$	$0.0164^{+0.0009}_{-0.0005}$	$0.0905^{+0.0010}_{-0.0010}$	$2.32^{+0.13}_{-0.08}$	1046^{+12}_{-12}	$8.1^{+2.3}_{-2.4}$	$2.3^{+0.7}_{-0.7}$	$0.8^{+0.2}_{-0.5}$	4×10^{-4}	VP
201437844.02	HD 106315 c	$21.05788^{+0.00132}_{-0.00133}$	$2757.0732^{+0.0021}_{-0.0020}$	$34.7^{+1.2}_{-3.5}$	$0.27^{+0.24}_{-0.19}$	$0.0305^{+0.0006}_{-0.0004}$	$0.1533^{+0.0016}_{-0.0017}$	$4.31^{+0.10}_{-0.08}$	804^{+9}_{-9}	$17.8^{+3.7}_{-3.4}$	$3.9^{+0.8}_{-0.7}$	$1.3^{+0.1}_{-0.3}$	4×10^{-5}	VP
201595106.01		$0.87703^{+0.00011}_{-0.00013}$	$2750.0513^{+0.0050}_{-0.0048}$	$5.4^{+1.3}_{-1.3}$	$0.41^{+0.32}_{-0.28}$	$0.0114^{+0.0011}_{-0.0009}$	$0.0181^{+0.0001}_{-0.0001}$	$1.20^{+0.11}_{-0.10}$	1874^{+16}_{-16}	$2.9^{+1.8}_{-1.6}$	$1.9^{+1.2}_{-1.1}$	$2.7^{+2.4}_{-1.5}$	2×10^{-3}	PC
201598502.01	K2-153 b	$7.51574^{+0.00205}_{-0.00240}$	$2755.4270^{+0.0134}_{-0.0111}$	$23.6^{+5.5}_{-6.7}$	$0.42^{+0.35}_{-0.29}$	$0.0348^{+0.0037}_{-0.0032}$	$0.0614^{+0.0004}_{-0.0004}$	$2.00^{+0.21}_{-0.18}$	497^{+6}_{-6}	$6.7^{+2.6}_{-2.5}$	$3.3^{+1.3}_{-1.2}$	$3.1^{+2.7}_{-2.0}$	5×10^{-5}	VP
201615463.01	K2-166 b	$8.52695^{+0.00362}_{-0.00370}$	$2753.7635^{+0.0165}_{-0.0167}$	$11.1^{+1.2}_{-2.6}$	$0.40^{+0.32}_{-0.28}$	$0.0124^{+0.0011}_{-0.0010}$	$0.0858^{+0.0010}_{-0.0009}$	$2.19^{+0.20}_{-0.19}$	1140^{+17}_{-18}	$7.4^{+2.5}_{-2.4}$	$2.1^{+0.7}_{-0.7}$	$0.3^{+0.1}_{-0.1}$	3×10^{-4}	VP
228707509.01		$15.35092^{+0.00032}_{-0.00033}$	$2752.5093^{+0.0010}_{-0.0009}$	$25.3^{+1.4}_{-1.1}$	$0.63^{+0.04}_{-0.06}$	$0.1505^{+0.0026}_{-0.0031}$	$0.1210^{+0.0027}_{-0.0029}$	$16.31^{+0.75}_{-0.72}$	734^{+32}_{-33}	$98.8^{+59.6}_{-36.1}$	$25.4^{+15.3}_{-9.3}$	$0.9^{+0.2}_{-0.1}$	7×10^{-4}	PC
228720681.01		$15.78132^{+0.00038}_{-0.00037}$	$2753.4189^{+0.0010}_{-0.0010}$	$26.1^{+4.0}_{-2.3}$	$0.68^{+0.07}_{-0.15}$	$0.0982^{+0.0026}_{-0.0035}$	$0.1182^{+0.0013}_{-0.0014}$	$10.87^{+1.55}_{-1.53}$	741^{+52}_{-54}	$56.7^{+29.8}_{-18.5}$	$15.7^{+8.3}_{-5.1}$	$1.0^{+0.5}_{-0.2}$	1×10^{-2}	PC
228721452.01	K2-223 b	$0.50565^{+0.00006}_{-0.00005}$	$2750.5640^{+0.0042}_{-0.0049}$	$3.9^{+1.1}_{-0.9}$	$0.41^{+0.32}_{-0.28}$	$0.0083^{+0.0009}_{-0.0007}$	$0.0127^{+0.0001}_{-0.0001}$	$0.89^{+0.10}_{-0.08}$	2271^{+23}_{-23}	$0.9^{+0.8}_{-0.6}$	$0.7^{+0.6}_{-0.4}$	$3.0^{+3.2}_{-1.7}$	1×10^{-4}	VP
228721452.02	K2-223 c	$4.56327^{+0.00051}_{-0.00049}$	$2749.9755^{+0.0044}_{-0.0045}$	$11.0^{+1.2}_{-2.6}$	$0.42^{+0.30}_{-0.29}$	$0.0146^{+0.0010}_{-0.0006}$	$0.0549^{+0.0003}_{-0.0003}$	$1.57^{+0.11}_{-0.07}$	1091^{+11}_{-11}	$5.0^{+2.4}_{-2.2}$	$1.8^{+0.9}_{-0.8}$	$0.8^{+0.3}_{-0.5}$	2×10^{-6}	VP
228724899.01		$5.20256^{+0.00042}_{-0.00044}$	$2753.4559^{+0.0036}_{-0.0034}$	$26.2^{+3.5}_{-6.5}$	$0.42^{+0.32}_{-0.29}$	$0.0338^{+0.0028}_{-0.0019}$	$0.0578^{+0.0005}_{-0.0005}$	$3.58^{+0.31}_{-0.20}$	1000^{+14}_{-14}	$14.1^{+3.2}_{-2.9}$	$5.4^{+1.2}_{-1.1}$	$8.9^{+4.0}_{-5.1}$	1×10^{-1}	PC
228725791.01	K2-247 b	$2.25021^{+0.00033}_{-0.00036}$	$2749.9770^{+0.0064}_{-0.0061}$	$8.7^{+1.5}_{-2.4}$	$0.43^{+0.34}_{-0.30}$	$0.0283^{+0.0025}_{-0.0020}$	$0.0304^{+0.0004}_{-0.0004}$	$2.12^{+0.19}_{-0.16}$	979^{+52}_{-51}	$7.3^{+2.5}_{-2.5}$	$4.3^{+1.5}_{-1.5}$	$1.7^{+1.1}_{-1.1}$	2×10^{-9}	VP
228725791.02	K2-247 c	$6.49424^{+0.00260}_{-0.00251}$	$2755.1369^{+0.0176}_{-0.0163}$	$18.2^{+3.9}_{-4.7}$	$0.41^{+0.33}_{-0.28}$	$0.0292^{+0.0032}_{-0.0030}$	$0.0615^{+0.0008}_{-0.0008}$	$2.19^{+0.25}_{-0.23}$	688^{+36}_{-35}	$7.5^{+2.6}_{-2.5}$	$3.1^{+1.1}_{-1.1}$	$1.9^{+1.5}_{-1.1}$	1×10^{-7}	VP
228725972.01	K2-224 b	$4.47904^{+0.00116}_{-0.00132}$	$2752.6719^{+0.0135}_{-0.0111}$	$13.2^{+2.5}_{-3.5}$	$0.41^{+0.34}_{-0.28}$	$0.0170^{+0.0017}_{-0.0015}$	$0.0516^{+0.0004}_{-0.0004}$	$1.56^{+0.16}_{-0.14}$	1002^{+11}_{-11}	$4.9^{+2.4}_{-2.3}$	$2.0^{+1.0}_{-0.9}$	$1.5^{+1.1}_{-0.9}$	2×10^{-6}	VP
228725972.02	K2-224 c	$10.09489^{+0.00119}_{-0.00114}$	$2755.4157^{+0.0041}_{-0.0041}$	$20.3^{+1.8}_{-4.5}$	$0.40^{+0.31}_{-0.27}$	$0.0262^{+0.0017}_{-0.0012}$	$0.0886^{+0.0007}_{-0.0007}$	$2.41^{+0.16}_{-0.12}$	764^{+9}_{-9}	$8.4^{+2.4}_{-2.5}$	$2.7^{+0.7}_{-0.8}$	$1.1^{+0.3}_{-0.6}$	9×10^{-6}	VP
228729473.01		$16.77217^{+0.00185}_{-0.00192}$	$2752.7609^{+0.0039}_{-0.0036}$	$6.8^{+1.5}_{-1.0}$	$0.63^{+0.13}_{-0.34}$	$0.0448^{+0.0022}_{-0.0025}$	$0.1367^{+0.0038}_{-0.0041}$	$19.29^{+1.18}_{-1.11}$	1173^{+26}_{-27}	$120.7^{+80.6}_{-47.8}$	$26.4^{+17.9}_{-10.5}$	< 0.05	2×10^{-1}	FP
228732031.01	K2-131 b	$0.36931^{+0.00001}_{-0.00001}$	$2749.9355^{+0.0011}_{-0.0010}$	$2.6^{+0.2}_{-0.4}$	$0.40^{+0.27}_{-0.26}$	$0.0207^{+0.0010}_{-0.0005}$	$0.0095^{+0.0000}_{-0.0000}$	$1.70^{+0.09}_{-0.05}$	2062^{+23}_{-23}	$5.5^{+2.3}_{-2.3}$	$5.4^{+2.3}_{-2.2}$	$1.7^{+0.4}_{-0.6}$	2×10^{-9}	VP
228734900.01	K2-225 b	$15.87209^{+0.00387}_{-0.00338}$	$2754.3754^{+0.0091}_{-0.0081}$	$17.8^{+1.9}_{-4.1}$	$0.40^{+0.32}_{-0.27}$	$0.0188^{+0.0013}_{-0.0010}$	$0.1340^{+0.0010}_{-0.0010}$	$3.49^{+0.26}_{-0.20}$	902^{+13}_{-13}	$13.6^{+3.1}_{-2.8}$	$2.9^{+0.7}_{-0.6}$	$0.3^{+0.1}_{-0.2}$	4×10^{-3}	VP
228735255.01	K2-140 b	$6.56918^{+0.00044}_{-0.00004}$	$2755.2851^{+0.0002}_{-0.0002}$	$15.1^{+0.1}_{-0.3}$	$0.12^{+0.10}_{-0.08}$	$0.1130^{+0.0006}_{-0.0005}$	$0.0687^{+0.0005}_{-0.0005}$	$12.25^{+0.17}_{-0.17}$	957^{+11}_{-11}	$67.2^{+31.2}_{-21.4}$	$22.8^{+10.7}_{-7.3}$	$1.1^{+0.0}_{-0.1}$	1×10^{-14}	VP

Table 5 continued

Table 5 *(continued)*

EPIC	Name	$P_{\rm orb}$ [days]	T_0 [BKJD]	a [$R_\star$]	b	R_p [$R_\star$]	a [AU]	R_p [$R_\oplus$]	$T_{\rm eq}$ [K]	M_P [$M_\oplus$]	$K_{\rm pred}$ [m s^{-1}]	$\rho_{\star,LC}$ [$\rho_\odot$]	FPP	Disposition
228736155.01	K2-226 b	$3.27108^{+0.00049}_{-0.00050}$	$2751.0247^{+0.0062}_{-0.0059}$	$9.7^{+1.2}_{-2.7}$	$0.45^{+0.33}_{-0.31}$	$0.0156^{+0.0013}_{-0.0009}$	$0.0413^{+0.0005}_{-0.0005}$	$1.54^{+0.14}_{-0.09}$	1120^{+16}_{-16}	$4.9^{+2.4}_{-2.2}$	$2.3^{+1.1}_{-1.0}$	$1.1^{+0.5}_{-0.7}$	2×10^{-7}	VP
228739306.01	K2-248 b	$7.17256^{+0.00148}_{-0.00142}$	$2755.1042^{+0.0072}_{-0.0078}$	$16.2^{+1.8}_{-3.9}$	$0.40^{+0.33}_{-0.28}$	$0.0255^{+0.0019}_{-0.0013}$	$0.0699^{+0.0010}_{-0.0010}$	$2.57^{+0.20}_{-0.14}$	886^{+19}_{-18}	$9.2^{+2.5}_{-2.4}$	$3.3^{+0.9}_{-0.9}$	$1.1^{+0.4}_{-0.6}$	6×10^{-5}	VP
228748383.01	K2-249 b	$12.40900^{+0.00337}_{-0.00284}$	$2750.0457^{+0.0106}_{-0.0113}$	$14.5^{+1.7}_{-3.6}$	$0.41^{+0.33}_{-0.28}$	$0.0162^{+0.0014}_{-0.0011}$	$0.1151^{+0.0030}_{-0.0031}$	$2.79^{+0.27}_{-0.22}$	1061^{+66}_{-66}	$10.1^{+2.8}_{-2.7}$	$2.3^{+0.6}_{-0.6}$	$0.3^{+0.1}_{-0.2}$	1×10^{-4}	VP
228748826.01	K2-250 b	$4.01457^{+0.00062}_{-0.00057}$	$2751.1212^{+0.0061}_{-0.0066}$	$12.3^{+1.5}_{-3.0}$	$0.41^{+0.32}_{-0.28}$	$0.0276^{+0.0022}_{-0.0016}$	$0.0459^{+0.0005}_{-0.0005}$	$2.44^{+0.19}_{-0.15}$	958^{+14}_{-13}	$8.6^{+2.5}_{-2.5}$	$4.0^{+1.2}_{-1.1}$	$1.6^{+0.6}_{-0.9}$	3×10^{-5}	VP
228753871.01		$18.69646^{+0.00447}_{-0.00441}$	$2757.7290^{+0.0108}_{-0.0108}$	$65.6^{+11.6}_{-17.2}$	$0.42^{+0.34}_{-0.29}$	$0.0278^{+0.0028}_{-0.0024}$	$0.1302^{+0.0014}_{-0.0014}$	$2.35^{+0.25}_{-0.20}$	571^{+19}_{-19}	$8.2^{+2.6}_{-2.6}$	$2.2^{+0.7}_{-0.7}$	$10.8^{+6.9}_{-6.5}$	7×10^{-2}	PC
228758778.01	K2-251 b	$9.30075^{+0.00332}_{-0.00321}$	$2756.0782^{+0.0128}_{-0.0108}$	$20.6^{+4.9}_{-6.1}$	$0.44^{+0.33}_{-0.30}$	$0.0437^{+0.0047}_{-0.0038}$	$0.0694^{+0.0005}_{-0.0005}$	$2.35^{+0.26}_{-0.21}$	437^{+9}_{-9}	$8.2^{+2.6}_{-2.5}$	$3.9^{+1.2}_{-1.2}$	$1.4^{+1.2}_{-0.9}$	4×10^{-7}	VP
228758948.01		$12.20239^{+0.00072}_{-0.00070}$	$2753.8291^{+0.0024}_{-0.0023}$	$22.2^{+1.8}_{-4.6}$	$0.40^{+0.29}_{-0.26}$	$0.0370^{+0.0018}_{-0.0010}$	$0.1066^{+0.0006}_{-0.0006}$	$4.15^{+0.21}_{-0.14}$	812^{+10}_{-9}	$17.0^{+3.5}_{-3.3}$	$4.5^{+0.9}_{-0.9}$	$1.0^{+0.3}_{-0.5}$	4×10^{-4}	PC
228763938.01	K2-252 b	$13.81513^{+0.00461}_{-0.00448}$	$2763.1901^{+0.0118}_{-0.0111}$	$25.7^{+3.5}_{-6.3}$	$0.41^{+0.32}_{-0.28}$	$0.0193^{+0.0018}_{-0.0013}$	$0.1041^{+0.0008}_{-0.0007}$	$1.74^{+0.17}_{-0.12}$	639^{+7}_{-7}	$5.6^{+2.4}_{-2.3}$	$1.8^{+0.7}_{-0.7}$	$1.2^{+0.6}_{-0.7}$	4×10^{-5}	VP
228784812.01		$4.18787^{+0.00138}_{-0.00137}$	$2751.0327^{+0.0115}_{-0.0121}$	$12.5^{+0.6}_{-0.6}$	$0.56^{+0.26}_{-0.31}$	$0.0124^{+0.0020}_{-0.0016}$	$0.0510^{+0.0012}_{-0.0012}$	$1.36^{+0.22}_{-0.19}$	1142^{+47}_{-43}	$3.9^{+2.5}_{-2.2}$	$1.5^{+1.0}_{-0.9}$	$1.5^{+0.2}_{-0.2}$	2×10^{-1}	PC
228798746.01	K2-228 b	$2.69828^{+0.00022}_{-0.00022}$	$2750.1943^{+0.0039}_{-0.0041}$	$12.2^{+1.3}_{-2.7}$	$0.42^{+0.30}_{-0.29}$	$0.0170^{+0.0013}_{-0.0008}$	$0.0338^{+0.0003}_{-0.0003}$	$1.21^{+0.10}_{-0.06}$	914^{+14}_{-13}	$3.2^{+1.7}_{-1.7}$	$1.8^{+1.0}_{-1.0}$	$3.3^{+1.2}_{-1.8}$	1×10^{-3}	VP
228801451.01	K2-229 b	$0.58426^{+0.00002}_{-0.00002}$	$2750.4691^{+0.0012}_{-0.0012}$	$3.4^{+0.2}_{-0.6}$	$0.38^{+0.28}_{-0.26}$	$0.0133^{+0.0007}_{-0.0004}$	$0.0131^{+0.0000}_{-0.0000}$	$1.14^{+0.06}_{-0.03}$	1818^{+14}_{-15}	$2.7^{+1.3}_{-1.5}$	$2.2^{+1.1}_{-1.3}$	$1.5^{+0.4}_{-0.6}$	4×10^{-10}	VP
228801451.02	K2-229 c	$8.32727^{+0.00041}_{-0.00043}$	$2753.3431^{+0.0019}_{-0.0019}$	$24.9^{+2.0}_{-5.0}$	$0.39^{+0.29}_{-0.27}$	$0.0236^{+0.0015}_{-0.0007}$	$0.0769^{+0.0003}_{-0.0003}$	$2.03^{+0.12}_{-0.06}$	750^{+6}_{-6}	$6.9^{+2.3}_{-2.4}$	$2.4^{+0.8}_{-0.8}$	$3.0^{+0.8}_{-1.5}$	5×10^{-5}	VP
228804845.01	K2-230 b	$2.86041^{+0.00061}_{-0.00061}$	$2749.5918^{+0.0093}_{-0.0091}$	$7.3^{+1.4}_{-1.6}$	$0.39^{+0.31}_{-0.26}$	$0.0129^{+0.0011}_{-0.0010}$	$0.0409^{+0.0003}_{-0.0002}$	$1.96^{+0.18}_{-0.16}$	1529^{+22}_{-22}	$6.5^{+2.4}_{-2.4}$	$2.7^{+1.0}_{-1.0}$	$0.6^{+0.4}_{-0.3}$	7×10^{-5}	VP
228809391.01		$19.57833^{+0.00492}_{-0.00484}$	$2763.8040^{+0.0074}_{-0.0076}$	$52.5^{+5.9}_{-12.5}$	$0.42^{+0.31}_{-0.29}$	$0.0272^{+0.0020}_{-0.0016}$	$0.1408^{+0.0015}_{-0.0015}$	$2.77^{+0.21}_{-0.17}$	644^{+10}_{-10}	$10.1^{+2.6}_{-2.5}$	$2.4^{+0.6}_{-0.6}$	$5.1^{+1.9}_{-2.8}$	2×10^{-2}	PC
228809550.01	K2-253 b	$4.00167^{+0.00013}_{-0.00013}$	$2750.9993^{+0.0013}_{-0.0014}$	$13.9^{+0.8}_{-2.0}$	$0.34^{+0.26}_{-0.23}$	$0.1050^{+0.0046}_{-0.0024}$	$0.0506^{+0.0010}_{-0.0011}$	$12.67^{+0.69}_{-0.61}$	1238^{+57}_{-53}	$70.8^{+34.9}_{-23.2}$	$27.0^{+13.6}_{-8.8}$	$2.2^{+0.4}_{-0.8}$	3×10^{-4}	VP
228834632.01		$11.73677^{+0.00795}_{-0.00854}$	$2758.6048^{+0.0292}_{-0.0299}$	$35.6^{+1.6}_{-1.7}$	$0.21^{+0.24}_{-0.15}$	$0.0270^{+0.0033}_{-0.0038}$	$0.0875^{+0.0009}_{-0.0010}$	$1.82^{+0.23}_{-0.26}$	516^{+17}_{-16}	$5.9^{+2.7}_{-2.7}$	$2.2^{+1.0}_{-1.0}$	$4.4^{+0.6}_{-0.6}$	2×10^{-2}	PC
228836835.01		$0.72813^{+0.00020}_{-0.00017}$	$2750.2622^{+0.0091}_{-0.0098}$	$7.4^{+0.7}_{-0.9}$	$0.49^{+0.34}_{-0.33}$	$0.0273^{+0.0057}_{-0.0060}$	$0.0121^{+0.0001}_{-0.0001}$	$1.27^{+0.27}_{-0.28}$	932^{+17}_{-17}	$3.3^{+2.8}_{-2.5}$	$4.0^{+3.4}_{-3.0}$	$10.2^{+3.3}_{-3.2}$	4×10^{-2}	PC
228846243.01		$25.58142^{+0.02417}_{-0.01921}$	$2756.8674^{+0.0336}_{-0.0348}$	$22.2^{+5.9}_{-7.3}$	$0.47^{+0.35}_{-0.31}$	$0.0406^{+0.0052}_{-0.0039}$	$0.1931^{+0.0045}_{-0.0047}$	$8.35^{+1.23}_{-0.93}$	914^{+67}_{-64}	$41.4^{+18.3}_{-12.0}$	$6.9^{+3.1}_{-2.0}$	$0.2^{+0.2}_{-0.2}$	9×10^{-2}	PC
228849382.01	K2-254 b	$4.09639^{+0.00081}_{-0.00079}$	$2749.9757^{+0.0096}_{-0.0106}$	$15.8^{+0.7}_{-0.8}$	$0.72^{+0.12}_{-0.26}$	$0.0223^{+0.0037}_{-0.0032}$	$0.0448^{+0.0005}_{-0.0005}$	$1.63^{+0.28}_{-0.24}$	791^{+26}_{-26}	$5.2^{+2.6}_{-2.4}$	$2.6^{+1.3}_{-1.2}$	$3.2^{+0.4}_{-0.4}$	2×10^{-4}	VP
228849382.02	K2-254 c	$12.11839^{+0.00303}_{-0.00321}$	$2757.6136^{+0.0101}_{-0.0104}$	$31.3^{+4.8}_{-8.0}$	$0.42^{+0.33}_{-0.29}$	$0.0298^{+0.0032}_{-0.0024}$	$0.0923^{+0.0010}_{-0.0010}$	$2.19^{+0.24}_{-0.18}$	551^{+18}_{-18}	$7.5^{+2.5}_{-2.4}$	$2.6^{+0.9}_{-0.9}$	$2.8^{+1.5}_{-1.6}$	2×10^{-6}	VP
228888935.01		$5.69046^{+0.00027}_{-0.00028}$	$2751.6711^{+0.0020}_{-0.0021}$	$8.1^{+2.5}_{-0.9}$	$0.76^{+0.06}_{-0.24}$	$0.0881^{+0.0032}_{-0.0062}$	$0.0707^{+0.0017}_{-0.0018}$	$18.81^{+1.20}_{-1.35}$	1503^{+109}_{-106}	$115.3^{+76.5}_{-44.1}$	$32.1^{+21.6}_{-12.4}$	$0.2^{+0.3}_{-0.1}$	1×10^{-1}	PC
228894622.01	K2-255 b	$1.96417^{+0.00004}_{-0.00004}$	$2750.3015^{+0.0008}_{-0.0008}$	$9.1^{+0.9}_{-2.3}$	$0.44^{+0.31}_{-0.31}$	$0.0386^{+0.0038}_{-0.0013}$	$0.0274^{+0.0003}_{-0.0003}$	$2.90^{+0.28}_{-0.11}$	1034^{+17}_{-17}	$10.8^{+2.6}_{-2.5}$	$6.9^{+1.7}_{-1.6}$	$2.6^{+0.9}_{-1.5}$	1×10^{-7}	VP
228934525.01	K2-154 b	$3.67626^{+0.00030}_{-0.00031}$	$2752.0533^{+0.0037}_{-0.0035}$	$14.5^{+1.9}_{-3.9}$	$0.44^{+0.33}_{-0.30}$	$0.0288^{+0.0031}_{-0.0015}$	$0.0405^{+0.0003}_{-0.0003}$	$1.99^{+0.21}_{-0.11}$	715^{+9}_{-8}	$6.8^{+2.5}_{-2.4}$	$3.7^{+1.4}_{-1.3}$	$3.0^{+1.4}_{-1.8}$	5×10^{-10}	VP
228934525.02	K2-154 c	$7.95486^{+0.00084}_{-0.00085}$	$2751.3376^{+0.0048}_{-0.0043}$	$24.9^{+2.8}_{-5.8}$	$0.42^{+0.31}_{-0.27}$	$0.0300^{+0.0025}_{-0.0019}$	$0.0677^{+0.0005}_{-0.0005}$	$2.07^{+0.18}_{-0.13}$	552^{+7}_{-7}	$7.0^{+2.4}_{-2.4}$	$3.0^{+1.0}_{-1.0}$	$3.3^{+1.3}_{-1.8}$	2×10^{-9}	VP
228964773.01		$37.20364^{+0.01391}_{-0.01725}$	$2776.7633^{+0.0124}_{-0.0115}$	$55.7^{+9.6}_{-15.3}$	$0.42^{+0.33}_{-0.29}$	$0.0543^{+0.0055}_{-0.0046}$	$0.2095^{+0.0021}_{-0.0021}$	$5.10^{+0.54}_{-0.46}$	498^{+10}_{-10}	$22.0^{+6.7}_{-4.8}$	$4.6^{+1.4}_{-1.0}$	$1.7^{+1.0}_{-1.0}$	1×10^{-2}	PC
228968232.01	K2-256 b	$5.52011^{+0.00239}_{-0.00289}$	$2753.5247^{+0.0202}_{-0.0191}$	$7.6^{+1.3}_{-1.9}$	$0.42^{+0.34}_{-0.29}$	$0.0309^{+0.0028}_{-0.0022}$	$0.0578^{+0.0008}_{-0.0008}$	$2.63^{+0.25}_{-0.21}$	845^{+28}_{-28}	$9.4^{+2.7}_{-2.6}$	$3.8^{+1.1}_{-1.0}$	$0.2^{+0.1}_{-0.1}$	1×10^{-5}	VP
228974324.01	K2-257 b	$1.60588^{+0.00014}_{-0.00013}$	$2750.2875^{+0.0035}_{-0.0038}$	$8.2^{+1.1}_{-1.8}$	$0.40^{+0.31}_{-0.27}$	$0.0153^{+0.0011}_{-0.0008}$	$0.0216^{+0.0002}_{-0.0002}$	$0.83^{+0.06}_{-0.05}$	789^{+14}_{-14}	$0.7^{+0.5}_{-0.4}$	$0.6^{+0.4}_{-0.4}$	$2.9^{+1.3}_{-1.5}$	7×10^{-11}	VP
228974907.01		$20.84919^{+0.02660}_{-0.03161}$	$2759.6108^{+0.0550}_{-0.0467}$	$33.9^{+7.8}_{-12.5}$	$0.41^{+0.35}_{-0.29}$	$0.0103^{+0.0011}_{-0.0011}$	$0.1828^{+0.0012}_{-0.0012}$	$3.01^{+0.33}_{-0.32}$	1349^{+50}_{-49}	$11.1^{+3.1}_{-2.9}$	$1.7^{+0.5}_{-0.4}$	$1.2^{+1.0}_{-0.9}$	5×10^{-3}	PC
229004835.01		$16.13655^{+0.00168}_{-0.00182}$	$2764.6294^{+0.0039}_{-0.0035}$	$54.6^{+4.8}_{-10.7}$	$0.38^{+0.30}_{-0.27}$	$0.0184^{+0.0010}_{-0.0007}$	$0.1218^{+0.0005}_{-0.0005}$	$2.02^{+0.12}_{-0.08}$	739^{+7}_{-7}	$6.8^{+2.3}_{-2.3}$	$1.8^{+0.6}_{-0.6}$	$8.4^{+2.4}_{-4.0}$	2×10^{-2}	PC
229017395.01	K2-258 b	$19.09210^{+0.00576}_{-0.00633}$	$2753.2928^{+0.0147}_{-0.0128}$	$21.5^{+2.0}_{-4.5}$	$0.37^{+0.32}_{-0.25}$	$0.0210^{+0.0014}_{-0.0013}$	$0.1490^{+0.0025}_{-0.0026}$	$3.00^{+0.21}_{-0.20}$	831^{+30}_{-30}	$11.1^{+2.6}_{-2.7}$	$2.3^{+0.6}_{-0.6}$	$0.4^{+0.1}_{-0.2}$	2×10^{-4}	VP
229103251.01		$11.67254^{+0.00454}_{-0.00402}$	$2756.7039^{+0.0131}_{-0.0140}$	$28.3^{+8.6}_{-9.0}$	$0.44^{+0.36}_{-0.30}$	$0.0283^{+0.0033}_{-0.0025}$	$0.1057^{+0.0023}_{-0.0024}$	$3.87^{+0.47}_{-0.36}$	946^{+43}_{-44}	$15.6^{+4.2}_{-3.4}$	$4.0^{+1.1}_{-0.9}$	$2.2^{+2.7}_{-1.5}$	6×10^{-1}	PC
229131722.01	K2-259 b	$15.48043^{+0.00332}_{-0.00392}$	$2752.7094^{+0.0100}_{-0.0102}$	$29.9^{+4.4}_{-7.1}$	$0.41^{+0.33}_{-0.28}$	$0.0189^{+0.0015}_{-0.0013}$	$0.1271^{+0.0010}_{-0.0011}$	$2.32^{+0.20}_{-0.17}$	795^{+13}_{-13}	$8.1^{+2.5}_{-2.5}$	$1.9^{+0.6}_{-0.6}$	$1.5^{+0.8}_{-0.8}$	2×10^{-3}	VP
229133720.01		$4.03692^{+0.00013}_{-0.00014}$	$2750.9634^{+0.0013}_{-0.0012}$	$13.4^{+0.9}_{-2.3}$	$0.36^{+0.28}_{-0.25}$	$0.0285^{+0.0015}_{-0.0007}$	$0.0456^{+0.0005}_{-0.0005}$	$2.24^{+0.12}_{-0.07}$	870^{+29}_{-28}	$7.7^{+2.4}_{-2.3}$	$3.7^{+1.1}_{-1.1}$	$2.0^{+0.4}_{-0.9}$	5×10^{-8}	PC

Note—M_P is the mass predicted using the mass-radius relation of Wolfgang et al. (2016) (see Section 6.4). We note that this mass-radius relation was calibrated with sub-Neptunes similar in size to the vast majority of the planets in our validated sample; the predictions may not be accurate for larger candidates, but we report them here anyway for the sake of uniformity. The "Disposition" column indicates the final validation status of each candidate: "VP" = validated planet; "PC" = planet candidate; "FP" = false positive.

Table 6. Stellar parameters.

EPIC	$T_{\rm eff}$ [K]	log g [cgs]	[Fe/H] [dex]	Mass [$M_\odot$]	Radius [$R_\odot$]	Distance [pc]	$v \sin i$ [km/s]	Provenance
201092629	5262^{+43}_{-39}	4.54 ± 0.01	$-0.44^{+0.04}_{-0.03}$	0.71 ± 0.01	0.75 ± 0.01	$149.6^{+1.1}_{-1.0}$	2.08 ± 0.29	This work
201102594	3459^{+65}_{-38}	4.89 ± 0.01	$-0.01^{+0.16}_{-0.18}$	0.38 ± 0.01	0.37 ± 0.01	109.6 ± 0.6	—	—
201110617	4597 ± 50	$4.62^{+0.02}_{-0.01}$	-0.25 ± 0.06	$0.66^{+0.02}_{-0.01}$	0.66 ± 0.01	150.4 ± 1.0	1.80 ± 0.30	This work
201111557	5011^{+289}_{-239}	4.62 ± 0.01	-0.23 ± 0.23	$0.77^{+0.02}_{-0.03}$	0.71 ± 0.01	97.5 ± 0.5	—	—
201127519	4957^{+47}_{-49}	$4.58^{+0.02}_{-0.03}$	0.03 ± 0.05	0.81 ± 0.03	0.77 ± 0.01	118.0 ± 0.7	1.85 ± 0.22	This work
201128338	4044^{+34}_{-35}	4.67 ± 0.01	$0.12^{+0.09}_{-0.08}$	0.63 ± 0.01	0.61 ± 0.01	108.7 ± 0.4	—	Hirano et al. 2018
201132684	5503^{+51}_{-48}	4.45 ± 0.02	0.07 ± 0.07	$0.92^{+0.03}_{-0.02}$	0.95 ± 0.02	198.2 ± 2.1	—	Mayo et al. 2018
201164625	6264^{+83}_{-81}	3.66 ± 0.03	$0.18^{+0.02}_{-0.03}$	$1.78^{+0.06}_{-0.03}$	$3.30^{+0.13}_{-0.16}$	$1067.1^{+36.4}_{-53.7}$	11.50 ± 0.46	This work
201166680	6570^{+269}_{-171}	$4.26^{+0.02}_{-0.03}$	$-0.03^{+0.18}_{-0.19}$	$1.29^{+0.04}_{-0.06}$	1.39 ± 0.03	$269.2^{+3.6}_{-3.4}$	—	—
201180665	6234^{+210}_{-258}	$4.29^{+0.03}_{-0.05}$	$0.02^{+0.14}_{-0.17}$	$1.17^{+0.06}_{-0.09}$	1.28 ± 0.03	$611.6^{+9.3}_{-8.8}$	—	—
201211526	5677^{+38}_{-39}	4.44 ± 0.02	-0.29 ± 0.03	0.86 ± 0.02	$0.92^{+0.02}_{-0.01}$	$214.0^{+2.4}_{-2.3}$	3.69 ± 0.24	This work
201225286	5425 ± 44	$4.56^{+0.01}_{-0.02}$	-0.07 ± 0.06	$0.90^{+0.02}_{-0.03}$	0.83 ± 0.01	$171.9^{+1.4}_{-1.3}$	—	Mayo et al. 2018
201274010	5636^{+171}_{-124}	$4.53^{+0.01}_{-0.02}$	$-0.09^{+0.17}_{-0.21}$	$0.94^{+0.03}_{-0.04}$	0.88 ± 0.02	$510.3^{+8.6}_{-8.3}$	—	—
201352100	5108^{+61}_{-58}	4.60 ± 0.01	-0.08 ± 0.04	$0.83^{+0.01}_{-0.02}$	0.76 ± 0.01	203.5 ± 3.3	2.15 ± 0.30	This work
201357643	5793^{+66}_{-52}	4.16 ± 0.02	-0.45 ± 0.02	$0.83^{+0.02}_{-0.01}$	1.25 ± 0.03	$463.4^{+9.1}_{-8.4}$	4.62 ± 0.24	This work
201386739	5610^{+32}_{-29}	$4.43^{+0.04}_{-0.03}$	-0.19 ± 0.03	0.87 ± 0.02	0.94 ± 0.03	$723.1^{+24.9}_{-24.7}$	2.90 ± 0.30	This work
201390048	4842^{+49}_{-45}	4.63 ± 0.01	$-0.17^{+0.05}_{-0.06}$	0.75 ± 0.02	0.69 ± 0.01	125.1 ± 0.6	—	Mayo et al. 2018
201390927	5711^{+285}_{-273}	$4.42^{+0.06}_{-0.08}$	$0.01^{+0.15}_{-0.17}$	0.97 ± 0.09	$1.01^{+0.10}_{-0.08}$	$354.8^{+34.9}_{-30.1}$	—	—
201392505	5128^{+53}_{-54}	$4.60^{+0.01}_{-0.02}$	-0.16 ± 0.06	$0.81^{+0.02}_{-0.03}$	0.75 ± 0.01	$274.3^{+5.3}_{-5.0}$	2.46 ± 0.29	This work
201437844	6277^{+52}_{-51}	4.25 ± 0.02	-0.22 ± 0.07	$1.08^{+0.03}_{-0.04}$	1.29 ± 0.02	109.7 ± 0.7	12.90 ± 0.40	Rodriguez et al. 2017
201595106	5823 ± 19	$4.48^{+0.01}_{-0.02}$	-0.00 ± 0.03	$1.02^{+0.01}_{-0.02}$	$0.96^{+0.02}_{-0.01}$	$233.1^{+2.6}_{-2.4}$	3.62 ± 0.18	This work
201598502	3845 ± 37	4.73 ± 0.01	-0.09 ± 0.08	0.55 ± 0.01	0.53 ± 0.01	143.6 ± 0.9	—	Hirano et al. 2018
201615463	5960^{+52}_{-53}	4.09 ± 0.02	0.09 ± 0.06	$1.16^{+0.05}_{-0.03}$	1.61 ± 0.04	$481.0^{+9.7}_{-8.9}$	—	Mayo et al. 2018
228707509	5799^{+197}_{-241}	$4.44^{+0.04}_{-0.05}$	$0.00^{+0.16}_{-0.18}$	$1.00^{+0.06}_{-0.09}$	1.00 ± 0.04	$880.7^{+32.0}_{-29.7}$	—	—
228720681	5725^{+73}_{-76}	$4.37^{+0.13}_{-0.12}$	-0.27 ± 0.04	0.88 ± 0.03	$1.02^{+0.16}_{-0.13}$	$642.5^{+102.0}_{-82.3}$	12.00 ± 0.60	This work
228721452	5835^{+38}_{-40}	4.48 ± 0.01	0.12 ± 0.06	1.06 ± 0.02	0.99 ± 0.01	201.1 ± 2.5	—	Mayo et al. 2018
228724899	5533 ± 52	4.44 ± 0.02	0.17 ± 0.04	$0.95^{+0.03}_{-0.02}$	0.97 ± 0.02	$431.5^{+5.2}_{-5.0}$	2.90 ± 0.30	This work
228725791	4667^{+305}_{-183}	$4.63^{+0.01}_{-0.02}$	-0.08 ± 0.22	0.74 ± 0.03	$0.69^{+0.02}_{-0.01}$	260.2 ± 2.1	—	—
228725972	5620^{+42}_{-45}	$4.55^{+0.01}_{-0.02}$	-0.19 ± 0.06	0.91 ± 0.02	0.84 ± 0.01	277.7 ± 2.9	—	Mayo et al. 2018
228729473	4940^{+47}_{-41}	3.32 ± 0.04	-0.05 ± 0.02	$1.21^{+0.08}_{-0.14}$	$3.96^{+0.12}_{-0.11}$	$579.6^{+16.1}_{-14.6}$	3.46 ± 0.27	This work
228732031	5245^{+46}_{-52}	4.61 ± 0.01	-0.17 ± 0.03	0.84 ± 0.01	0.75 ± 0.01	$153.7^{+1.1}_{-1.0}$	4.30 ± 0.20	This work
228734900	5742^{+49}_{-47}	4.08 ± 0.02	0.38 ± 0.06	$1.27^{+0.02}_{-0.04}$	1.70 ± 0.04	$360.3^{+5.9}_{-5.7}$	—	Mayo et al. 2018
228735255	5705^{+50}_{-48}	4.45 ± 0.01	0.13 ± 0.04	1.00 ± 0.02	0.99 ± 0.01	$341.6^{+5.5}_{-5.1}$	3.80 ± 0.20	Giles et al. 2017
228736155	5424^{+48}_{-46}	4.47 ± 0.03	-0.03 ± 0.07	0.88 ± 0.03	0.91 ± 0.02	$211.2^{+3.4}_{-3.1}$	—	Mayo et al. 2018
228739306	5528^{+97}_{-86}	4.45 ± 0.03	-0.10 ± 0.04	$0.88^{+0.04}_{-0.03}$	0.92 ± 0.02	410.5 ± 4.9	2.60 ± 0.20	This work
228748383	6504^{+329}_{-419}	$4.16^{+0.05}_{-0.06}$	$0.04^{+0.14}_{-0.16}$	$1.32^{+0.09}_{-0.12}$	1.57 ± 0.06	$528.3^{+16.9}_{-14.7}$	—	—
228748826	5172^{+46}_{-44}	4.53 ± 0.03	-0.09 ± 0.04	$0.80^{+0.03}_{-0.02}$	0.81 ± 0.02	$417.6^{+6.2}_{-6.0}$	2.20 ± 0.30	This work
228753871	5312^{+190}_{-156}	$4.59^{+0.01}_{-0.02}$	$-0.18^{+0.16}_{-0.19}$	$0.84^{+0.02}_{-0.03}$	0.77 ± 0.01	295.9 ± 2.0	—	—
228758778	3717^{+85}_{-50}	4.76 ± 0.01	$-0.04^{+0.18}_{-0.19}$	0.52 ± 0.01	0.49 ± 0.01	147.7 ± 1.0	—	—
228758948	5931^{+42}_{-45}	$4.45^{+0.01}_{-0.02}$	0.11 ± 0.03	1.09 ± 0.02	1.03 ± 0.02	$446.2^{+7.5}_{-7.0}$	4.40 ± 0.20	This work
228763938	5152^{+41}_{-39}	$4.50^{+0.02}_{-0.01}$	-0.09 ± 0.04	$0.79^{+0.02}_{-0.01}$	0.82 ± 0.01	$229.9^{+2.1}_{-1.9}$	2.20 ± 0.20	This work
228784812	5815^{+187}_{-238}	$4.43^{+0.03}_{-0.05}$	$0.01^{+0.15}_{-0.19}$	$1.01^{+0.06}_{-0.09}$	$1.01^{+0.03}_{-0.02}$	$345.4^{+4.9}_{-5.0}$	—	—
228798746	4715^{+48}_{-46}	4.66 ± 0.01	-0.25 ± 0.06	0.71 ± 0.02	0.65 ± 0.01	142.4 ± 3.2	—	Mayo et al. 2018
228801451	5315^{+35}_{-31}	$4.59^{+0.00}_{-0.01}$	-0.09 ± 0.02	0.87 ± 0.01	0.79 ± 0.01	103.8 ± 1.0	2.46 ± 0.22	This work
228804845	5945^{+23}_{-25}	4.20 ± 0.02	0.10 ± 0.04	1.11 ± 0.02	1.39 ± 0.04	$548.9^{+14.3}_{-13.5}$	5.20 ± 0.20	This work
228809391	5674^{+63}_{-77}	$4.49^{+0.02}_{-0.03}$	-0.01 ± 0.03	0.97 ± 0.03	0.93 ± 0.02	$333.7^{+4.8}_{-4.7}$	3.20 ± 0.20	This work
228809550	6027^{+221}_{-240}	$4.39^{+0.03}_{-0.05}$	$-0.00^{+0.17}_{-0.19}$	$1.08^{+0.05}_{-0.08}$	1.10 ± 0.04	$901.8^{+30.0}_{-27.9}$	—	—
228834632	4395^{+135}_{-125}	4.67 ± 0.01	$-0.21^{+0.17}_{-0.18}$	0.65 ± 0.02	0.62 ± 0.01	285.3 ± 3.0	—	—
228836835	3562^{+70}_{-35}	4.83 ± 0.01	$-0.01^{+0.16}_{-0.18}$	0.45 ± 0.01	0.43 ± 0.01	$150.8^{+1.8}_{-1.7}$	—	—
228846243	6644^{+413}_{-454}	$4.05^{+0.05}_{-0.06}$	$0.06^{+0.14}_{-0.15}$	$1.47^{+0.10}_{-0.11}$	$1.89^{+0.11}_{-0.10}$	$1405.4^{+77.3}_{-70.8}$	—	—
228849382	4629^{+168}_{-123}	4.64 ± 0.01	$-0.14^{+0.18}_{-0.15}$	$0.71^{+0.02}_{-0.03}$	0.67 ± 0.01	229.4 ± 1.3	—	—
228888935	6452^{+452}_{-413}	4.01 ± 0.05	$0.08^{+0.13}_{-0.14}$	1.45 ± 0.11	1.97 ± 0.09	$1278.0^{+50.4}_{-46.9}$	—	—

Table 6 continued

Table 6 *(continued)*

EPIC	$T_{\rm eff}$ [K]	log g [cgs]	[Fe/H] [dex]	Mass [$M_\odot$]	Radius [$R_\odot$]	Distance [pc]	$v \sin i$ [km/s]	Provenance
228894622	4676^{+63}_{-61}	4.62 ± 0.02	$-0.14^{+0.07}_{-0.06}$	0.71 ± 0.03	0.69 ± 0.01	192.4 ± 1.5	2.46 ± 0.27	This work
228934525	4097^{+40}_{-45}	4.65 ± 0.01	$0.21^{+0.09}_{-0.10}$	$0.65^{+0.02}_{-0.01}$	0.63 ± 0.01	129.8 ± 0.4	—	Hirano et al. 2018
228964773	5574^{+64}_{-61}	$4.52^{+0.03}_{-0.04}$	-0.18 ± 0.03	0.89 ± 0.03	$0.86^{+0.03}_{-0.02}$	$802.5^{+25.3}_{-20.6}$	3.40 ± 0.20	This work
228968232	5219^{+179}_{-136}	$4.58^{+0.01}_{-0.02}$	-0.10 ± 0.17	$0.84^{+0.03}_{-0.04}$	0.78 ± 0.02	$580.5^{+14.9}_{-13.9}$	—	—
228974324	3725^{+80}_{-46}	4.76 ± 0.01	$-0.03^{+0.17}_{-0.18}$	0.52 ± 0.01	0.50 ± 0.01	64.1 ± 0.3	—	—
228974907	8003^{+370}_{-187}	3.86 ± 0.03	$-0.32^{+0.11}_{-0.14}$	$1.87^{+0.02}_{-0.05}$	$2.67^{+0.08}_{-0.11}$	$379.9^{+10.7}_{-11.2}$	—	—
229004835	5831^{+38}_{-35}	4.40 ± 0.02	-0.22 ± 0.01	0.92 ± 0.01	1.00 ± 0.01	$122.4^{+0.8}_{-0.9}$	3.77 ± 0.12	This work
229017395	6351^{+198}_{-228}	$4.29^{+0.03}_{-0.04}$	$0.01^{+0.15}_{-0.17}$	$1.21^{+0.05}_{-0.08}$	1.31 ± 0.03	$675.2^{+11.6}_{-11.5}$	—	—
229103251	6220^{+225}_{-305}	$4.30^{+0.03}_{-0.05}$	$0.02^{+0.15}_{-0.18}$	$1.16^{+0.07}_{-0.10}$	$1.26^{+0.04}_{-0.03}$	$756.2^{+15.0}_{-14.1}$	—	—
229131722	6059^{+62}_{-76}	$4.39^{+0.02}_{-0.03}$	0.16 ± 0.04	1.14 ± 0.03	$1.13^{+0.03}_{-0.02}$	$422.1^{+7.7}_{-7.8}$	5.23 ± 0.20	This work
229133720	4964^{+170}_{-139}	$4.61^{+0.01}_{-0.02}$	$-0.17^{+0.17}_{-0.16}$	$0.78^{+0.02}_{-0.03}$	0.72 ± 0.01	105.2 ± 0.5	—	—

Note— "Provenance" indicates the source of the spectroscopic parameters used as priors in our analysis (see Section 4.4). The $v \sin i$ uncertainties are internal to the *Kea* pipeline and do not account for other types of line broadening; thus they are likely to be underestimated.

Table 7. Individual false positive scenario likelihoods computed by `vespa`. Note: a – likelihood that the signal is due to a background eclipsing binary, at the measured period or twice that; b – likelihood that the signal is due to an eclipsing binary, at the measured period or twice that; c – likelihood that the signal is due to a hierarchical star system with an eclipsing component, at the measured period or twice that; d – likelihood that the signal is due to a planet.

EPIC	L_beb[a]	L_beb_Px2[a]	L_eb[b]	L_eb_Px2[b]	L_heb[c]	L_heb_Px2[c]	L_pl[d]	FPP
201092629.01	0	0	1.1×10^{-11}	7.8×10^{-10}	5.7×10^{-52}	1.4×10^{-20}	1.2×10^{-2}	6.8×10^{-8}
201102594.01	0	0	1.0×10^{-22}	1.1×10^{-13}	7.6×10^{-30}	2.9×10^{-21}	1.8×10^{-2}	5.9×10^{-12}
201110617.01	0	0	2.3×10^{-52}	4.5×10^{-13}	1.1×10^{-90}	3.7×10^{-42}	2.3×10^{-1}	2.0×10^{-12}
201111557.01	0	0	6.1×10^{-9}	1.2×10^{-6}	1.0×10^{-32}	2.4×10^{-14}	4.0×10^{-3}	3.0×10^{-4}
201127519.01	0	0	1.1×10^{-3}	3.2×10^{-6}	2.2×10^{-86}	4.6×10^{-27}	2.8×10^{-2}	3.9×10^{-2}
201128338.01	0	0	3.0×10^{-16}	2.0×10^{-10}	3.0×10^{-12}	1.1×10^{-12}	1.6×10^{-3}	1.3×10^{-7}
201132684.01	0	0	4.7×10^{-14}	3.4×10^{-9}	4.4×10^{-25}	2.3×10^{-12}	4.7×10^{-3}	7.2×10^{-7}
201132684.02	0	0	2.1×10^{-9}	5.6×10^{-8}	1.2×10^{-49}	1.4×10^{-18}	2.9×10^{-2}	2.0×10^{-6}
201164625.01	0	0	4.6×10^{-6}	3.0×10^{-7}	1.5×10^{-6}	5.0×10^{-7}	1.9×10^{-3}	3.6×10^{-3}
201166680.01	1.0×10^{-5}	3.3×10^{-6}	5.5×10^{-6}	2.3×10^{-6}	1.5×10^{-30}	2.8×10^{-16}	9.7×10^{-3}	2.2×10^{-3}
201166680.02	3.2×10^{-6}	1.5×10^{-6}	2.0×10^{-6}	9.0×10^{-8}	5.8×10^{-20}	5.8×10^{-13}	1.9×10^{-3}	3.6×10^{-3}
201180665.01	0	0	8.6×10^{-4}	1.7×10^{-6}	1.2×10^{-6}	1.6×10^{-8}	4.9×10^{-4}	6.4×10^{-1}
201211526.01	0	0	3.4×10^{-7}	3.6×10^{-6}	3.9×10^{-25}	3.2×10^{-12}	5.9×10^{-3}	6.7×10^{-4}
201225286.01	0	0	2.2×10^{-6}	2.1×10^{-6}	1.7×10^{-44}	1.8×10^{-13}	2.2×10^{-2}	1.9×10^{-4}
201274010.01	1.6×10^{-4}	2.8×10^{-4}	1.3×10^{-5}	1.6×10^{-5}	1.7×10^{-17}	2.7×10^{-10}	4.8×10^{-3}	8.9×10^{-2}
201352100.01	0	0	9.1×10^{-6}	3.1×10^{-5}	2.7×10^{-79}	8.2×10^{-22}	2.6×10^{-2}	1.5×10^{-3}
201357643.01	0	0	2.7×10^{-6}	4.4×10^{-6}	1.8×10^{-89}	4.4×10^{-24}	3.2×10^{-2}	2.2×10^{-4}
201386739.01	0	0	1.5×10^{-12}	1.8×10^{-7}	1.9×10^{-122}	5.9×10^{-29}	3.2×10^{-3}	5.7×10^{-5}
201390048.01	4.6×10^{-5}	5.8×10^{-6}	2.3×10^{-16}	8.5×10^{-9}	1.9×10^{-96}	2.1×10^{-24}	2.2×10^{-2}	2.3×10^{-3}
201390927.01	0	0	1.2×10^{-10}	4.2×10^{-8}	1.2×10^{-12}	1.6×10^{-9}	1.7×10^{-3}	2.6×10^{-5}
201392505.01	0	0	3.0×10^{-18}	1.2×10^{-11}	1.7×10^{-126}	1.2×10^{-38}	1.7×10^{-4}	7.0×10^{-8}
201437844.01	0	0	2.0×10^{-7}	1.7×10^{-5}	9.6×10^{-71}	5.1×10^{-20}	1.9×10^{-3}	8.7×10^{-3}
201437844.02	0	0	1.7×10^{-6}	1.4×10^{-7}	2.5×10^{-76}	2.5×10^{-34}	1.8×10^{-3}	1.0×10^{-3}
201595106.01	0	0	9.6×10^{-5}	3.9×10^{-4}	5.3×10^{-20}	2.9×10^{-12}	2.2×10^{-1}	2.2×10^{-3}
201598502.01	0	0	2.0×10^{-11}	4.8×10^{-7}	1.9×10^{-17}	3.7×10^{-10}	1.0×10^{-2}	4.7×10^{-5}
201615463.01	4.0×10^{-7}	1.3×10^{-6}	4.1×10^{-9}	6.1×10^{-9}	5.8×10^{-16}	6.0×10^{-10}	4.9×10^{-3}	3.4×10^{-4}
228707509.01	0	0	8.0×10^{-6}	1.3×10^{-7}	1.8×10^{-15}	6.0×10^{-19}	1.1×10^{-2}	7.4×10^{-4}
228720681.01	0	0	1.9×10^{-4}	1.2×10^{-6}	8.6×10^{-6}	1.2×10^{-10}	2.0×10^{-2}	1.0×10^{-2}
228721452.01	0	0	2.5×10^{-5}	2.7×10^{-4}	2.2×10^{-26}	9.2×10^{-22}	8.8×10^{-2}	3.3×10^{-3}
228721452.02	0	0	7.1×10^{-17}	3.8×10^{-7}	8.9×10^{-155}	4.6×10^{-23}	9.4×10^{-3}	4.1×10^{-5}
228724899.01	0	0	1.7×10^{-3}	1.7×10^{-4}	2.4×10^{-10}	6.3×10^{-7}	1.1×10^{-2}	1.4×10^{-1}
228725791.01	0	0	4.1×10^{-14}	1.9×10^{-9}	1.7×10^{-17}	5.1×10^{-13}	4.7×10^{-2}	4.0×10^{-8}
228725791.02	0	0	1.3×10^{-9}	4.7×10^{-8}	1.5×10^{-14}	1.7×10^{-10}	1.3×10^{-2}	3.7×10^{-6}
228725972.01	0	0	1.7×10^{-10}	8.4×10^{-7}	5.3×10^{-58}	9.1×10^{-15}	1.7×10^{-2}	5.0×10^{-5}

Table 7 continued

Table 7 *(continued)*

EPIC	L_beb[a]	L_beb_Px2[a]	L_eb[b]	L_eb_Px2[b]	L_heb[c]	L_heb_Px2[c]	L_pl[d]	FPP
228725972.02	0	0	4.2×10^{-10}	1.7×10^{-6}	8.6×10^{-70}	4.4×10^{-25}	7.6×10^{-3}	2.2×10^{-4}
228729473.01	0	0	2.3×10^{-3}	1.3×10^{-6}	2.7×10^{-77}	3.3×10^{-28}	8.0×10^{-3}	2.2×10^{-1}
228732031.01	0	0	6.5×10^{-43}	1.2×10^{-8}	9.9×10^{-62}	1.8×10^{-49}	7.5×10^{0}	1.6×10^{-9}
228734900.01	6.7×10^{-6}	4.7×10^{-6}	1.4×10^{-8}	2.6×10^{-7}	6.1×10^{-15}	1.8×10^{-10}	3.3×10^{-3}	3.5×10^{-3}
228735255.01	0	0	2.1×10^{-21}	1.4×10^{-16}	2.6×10^{-58}	7.2×10^{-31}	1.5×10^{-2}	9.5×10^{-15}
228736155.01	0	0	6.2×10^{-15}	8.0×10^{-9}	2.3×10^{-33}	1.7×10^{-12}	4.5×10^{-2}	1.8×10^{-7}
228739306.01	0	0	5.1×10^{-9}	2.5×10^{-6}	6.6×10^{-42}	2.1×10^{-17}	4.4×10^{-2}	5.6×10^{-5}
228748383.01	0	0	2.3×10^{-7}	9.9×10^{-9}	2.1×10^{-12}	6.3×10^{-12}	1.9×10^{-3}	1.3×10^{-4}
228748826.01	0	0	1.2×10^{-12}	2.5×10^{-6}	5.2×10^{-45}	7.9×10^{-19}	8.8×10^{-2}	2.8×10^{-5}
228753871.01	2.5×10^{-5}	2.7×10^{-5}	4.8×10^{-5}	5.0×10^{-6}	1.6×10^{-15}	3.7×10^{-10}	1.4×10^{-3}	7.0×10^{-2}
228758778.01	0	0	1.4×10^{-17}	1.3×10^{-9}	1.9×10^{-14}	3.3×10^{-13}	3.2×10^{-3}	4.1×10^{-7}
228758948.01	0	0	5.1×10^{-7}	9.1×10^{-6}	8.1×10^{-82}	1.6×10^{-24}	2.4×10^{-2}	4.1×10^{-4}
228763938.01	0	0	1.7×10^{-9}	1.7×10^{-7}	9.6×10^{-28}	5.6×10^{-13}	4.0×10^{-3}	4.5×10^{-5}
228784812.01	6.0×10^{-4}	1.4×10^{-3}	2.5×10^{-4}	1.7×10^{-4}	1.8×10^{-5}	1.0×10^{-5}	9.9×10^{-3}	2.0×10^{-1}
228798746.01	2.3×10^{-4}	5.7×10^{-6}	2.9×10^{-12}	4.4×10^{-7}	7.7×10^{-224}	3.7×10^{-39}	1.7×10^{-1}	1.4×10^{-3}
228801451.01	0	0	8.1×10^{-18}	1.7×10^{-9}	1.2×10^{-218}	1.4×10^{-102}	1.8×10^{-1}	9.4×10^{-9}
228801451.02	0	0	1.9×10^{-8}	2.7×10^{-5}	3.5×10^{-141}	2.0×10^{-16}	2.1×10^{-2}	1.3×10^{-3}
228804845.01	0	0	1.6×10^{-7}	7.8×10^{-7}	2.7×10^{-17}	2.2×10^{-11}	1.3×10^{-2}	7.2×10^{-5}
228809391.01	0	0	4.5×10^{-5}	1.3×10^{-6}	9.4×10^{-24}	4.6×10^{-14}	2.8×10^{-3}	1.6×10^{-2}
228809550.01	0	0	1.2×10^{-5}	2.9×10^{-6}	1.7×10^{-11}	7.1×10^{-8}	5.1×10^{-2}	3.0×10^{-4}
228834632.01	2.2×10^{-5}	5.1×10^{-5}	7.6×10^{-10}	3.7×10^{-8}	3.8×10^{-28}	2.1×10^{-13}	3.3×10^{-3}	2.2×10^{-2}
228836835.01	2.7×10^{-4}	1.4×10^{-3}	2.5×10^{-5}	1.8×10^{-4}	1.6×10^{-7}	2.6×10^{-6}	4.2×10^{-2}	4.3×10^{-2}
228846243.01	0	0	4.4×10^{-5}	3.6×10^{-5}	8.3×10^{-7}	1.3×10^{-6}	8.7×10^{-4}	8.6×10^{-2}
228849382.01	0	0	1.4×10^{-5}	4.9×10^{-5}	6.3×10^{-12}	5.8×10^{-8}	1.1×10^{-2}	6.0×10^{-3}
228849382.02	0	0	1.9×10^{-9}	1.4×10^{-7}	2.3×10^{-33}	1.6×10^{-13}	3.6×10^{-3}	3.9×10^{-5}
228888935.01	0	0	2.9×10^{-3}	1.1×10^{-5}	1.9×10^{-5}	4.2×10^{-7}	1.9×10^{-2}	1.3×10^{-1}
228894622.01	0	0	8.8×10^{-13}	2.6×10^{-8}	3.1×10^{-50}	5.6×10^{-24}	2.2×10^{-1}	1.2×10^{-7}
228934525.01	0	0	1.1×10^{-16}	9.8×10^{-10}	8.6×10^{-17}	5.5×10^{-10}	1.3×10^{-1}	1.2×10^{-8}
228934525.02	0	0	1.6×10^{-25}	2.1×10^{-14}	8.0×10^{-21}	5.1×10^{-11}	9.2×10^{-4}	5.5×10^{-8}
228964773.01	0	0	3.2×10^{-6}	7.6×10^{-6}	1.6×10^{-23}	6.6×10^{-12}	7.5×10^{-4}	1.4×10^{-2}
228968232.01	0	0	2.3×10^{-31}	1.8×10^{-9}	3.1×10^{-132}	1.6×10^{-33}	1.7×10^{-4}	1.0×10^{-5}
228974324.01	0	0	9.4×10^{-114}	5.0×10^{-12}	1.0×10^{-90}	2.3×10^{-24}	7.6×10^{-2}	6.6×10^{-11}
228974907.01	0	0	5.8×10^{-6}	2.4×10^{-7}	2.3×10^{-6}	9.7×10^{-7}	1.7×10^{-3}	5.5×10^{-3}
229004835.01	0	0	2.4×10^{-4}	1.8×10^{-6}	3.3×10^{-16}	6.0×10^{-9}	1.1×10^{-2}	2.2×10^{-2}
229017395.01	0	0	2.0×10^{-8}	6.2×10^{-8}	4.3×10^{-18}	5.1×10^{-12}	5.3×10^{-4}	1.5×10^{-4}
229103251.01	0	0	4.6×10^{-4}	1.9×10^{-4}	4.5×10^{-6}	4.3×10^{-6}	4.4×10^{-4}	6.0×10^{-1}
229131722.01	0	0	5.7×10^{-6}	1.6×10^{-6}	1.1×10^{-33}	3.1×10^{-14}	3.2×10^{-3}	2.2×10^{-3}
229133720.01	0	0	1.3×10^{-19}	2.2×10^{-8}	1.8×10^{-121}	3.9×10^{-25}	4.3×10^{-1}	5.1×10^{-8}

Table 8. Additional constraints to `vespa`. The columns "maxrad" and "secthresh" refer to the maximum radius (the angular size of the photometric aperture) and the secondary eclipse threshold (the maximum secondary eclipse depth allowed by the light curve), respectively.

EPIC	maxrad [arcsec]	secthresh
201092629.01	20.7	1×10^{-4}
201102594.01	15.1	2×10^{-4}
201110617.01	15.9	1×10^{-4}
201111557.01	17.5	1×10^{-4}
201127519.01	10.3	3×10^{-3}
201128338.01	18.3	2×10^{-4}
201132684.01	21.5	2×10^{-4}
201132684.02	21.5	3×10^{-4}

Table 8 continued

Table 8 *(continued)*

EPIC	maxrad [arcsec]	secthresh
201164625.01	19.1	1×10^{-5}
201166680.01	22.3	5×10^{-5}
201166680.02	22.3	1×10^{-4}
201180665.01	8.8	2×10^{-4}
201211526.01	13.5	8×10^{-5}
201225286.01	12.7	2×10^{-4}
201274010.01	16.7	2×10^{-4}
201352100.01	10.3	1×10^{-4}
201357643.01	6.4	1×10^{-4}
201386739.01	16.7	3×10^{-4}
201390048.01	10.3	2×10^{-4}
201390927.01	14.3	2×10^{-4}
201392505.01	8.0	1×10^{-3}
201437844.01	31.8	8×10^{-4}
201437844.02	31.8	2×10^{-4}
201595106.01	17.5	2×10^{-4}
201598502.01	15.1	3×10^{-4}
201615463.01	16.7	3×10^{-4}
228707509.01	14.3	3×10^{-4}
228720681.01	10.3	5×10^{-4}
228721452.01	14.3	5×10^{-5}

Table 8 continued

Table 8 *(continued)*

EPIC	maxrad [arcsec]	secthresh
228721452.02	14.3	5×10^{-5}
228724899.01	11.1	1×10^{-4}
228725791.01	11.9	5×10^{-4}
228725791.02	11.9	5×10^{-4}
228725972.01	14.3	2×10^{-4}
228725972.02	14.3	2×10^{-4}
228729473.01	19.1	2×10^{-4}
228732031.01	21.5	1×10^{-4}
228734900.01	15.9	6×10^{-4}
228735255.01	16.7	1×10^{-4}
228736155.01	15.1	1×10^{-4}
228739306.01	15.1	1×10^{-4}
228748383.01	15.9	2×10^{-4}
228748826.01	15.1	2×10^{-4}
228753871.01	13.5	1×10^{-4}
228758778.01	12.7	8×10^{-4}
228758948.01	17.5	2×10^{-4}
228763938.01	14.3	1×10^{-4}
228784812.01	8.8	5×10^{-5}
228798746.01	9.6	1×10^{-4}
228801451.01	18.3	1×10^{-4}
228801451.02	18.3	2×10^{-4}
228804845.01	19.1	1×10^{-4}
228809391.01	9.6	1×10^{-4}
228809550.01	11.1	3×10^{-4}
228834632.01	11.9	2×10^{-4}
228836835.01	8.0	1×10^{-4}
228846243.01	9.6	5×10^{-4}
228849382.01	8.0	3×10^{-4}
228849382.02	8.0	5×10^{-4}
228888935.01	8.8	2×10^{-3}
228894622.01	12.7	2×10^{-4}
228934525.01	9.6	2×10^{-4}
228934525.02	9.6	5×10^{-4}
228964773.01	7.2	8×10^{-4}
228968232.01	10.3	5×10^{-4}
228974324.01	11.9	1×10^{-4}
228974907.01	32.6	3×10^{-5}
229004835.01	11.1	3×10^{-5}
229017395.01	15.9	2×10^{-4}
229103251.01	16.7	1×10^{-4}
229131722.01	12.7	8×10^{-5}
229133720.01	18.3	2×10^{-4}

Table 9. WIYN/NESSI datasets used in this work.

EPIC	Filter center [nm]	Filter width [nm]	Obs. Date
201092629	562nm	44nm	2017-05-15
201092629	832nm	40nm	2017-05-15
201092629	562nm	44nm	2017-03-18
201092629	832nm	40nm	2017-03-18
201102594	562nm	44nm	2017-04-05
201102594	832nm	40nm	2017-04-05
201110617	832nm	40nm	2017-03-10
201110617	562nm	44nm	2017-03-10
201111557	562nm	44nm	2017-03-15
201111557	832nm	40nm	2017-03-15

Table 9 continued

Table 9 *(continued)*

EPIC	Filter center [nm]	Filter width [nm]	Obs. Date
201127519	562nm	44nm	2017-03-11
201127519	832nm	40nm	2017-03-11
201128338	832nm	40nm	2017-03-10
201128338	562nm	44nm	2017-03-10
201132684	832nm	40nm	2017-05-12
201132684	562nm	44nm	2017-05-12
201132684	562nm	44nm	2017-03-15
201132684	832nm	40nm	2017-03-15
201164625	562nm	44nm	2017-03-18
201164625	832nm	40nm	2017-03-18
201164625	562nm	44nm	2017-05-12
201164625	832nm	40nm	2017-05-12
201180665	832nm	40nm	2017-03-18
201180665	562nm	44nm	2017-03-18
201211526	832nm	40nm	2017-03-18
201211526	562nm	44nm	2017-03-18
201225286	562nm	44nm	2017-04-03
201225286	832nm	40nm	2017-04-03
201352100	562nm	44nm	2017-03-15
201352100	832nm	40nm	2017-03-15
201357643	562nm	44nm	2017-03-18
201357643	832nm	40nm	2017-03-18
201386739	562nm	44nm	2017-03-17
201386739	832nm	40nm	2017-03-17
201390927	832nm	40nm	2017-03-17
201390927	562nm	44nm	2017-03-17
201392505	832nm	40nm	2017-03-18
201392505	562nm	44nm	2017-03-18
201437844	562nm	44nm	2017-03-11
201437844	832nm	40nm	2017-03-11
201595106	832nm	40nm	2017-03-18
201595106	562nm	44nm	2017-03-18
201598502	832nm	40nm	2017-03-18
201598502	562nm	44nm	2017-03-18
228707509	562nm	44nm	2017-04-08
228707509	832nm	40nm	2017-04-08
228720681	832nm	40nm	2017-03-14
228720681	562nm	44nm	2017-03-14
228721452	562nm	44nm	2017-03-11
228721452	832nm	40nm	2017-03-11
228724899	562nm	44nm	2017-03-14
228724899	832nm	40nm	2017-03-14
228725791	562nm	44nm	2017-03-17
228725791	832nm	40nm	2017-03-17
228725972	832nm	40nm	2017-03-17
228725972	562nm	44nm	2017-03-17
228729473	832nm	40nm	2017-04-03
228729473	832nm	40nm	2017-05-19
228729473	562nm	44nm	2017-04-03
228729473	562nm	44nm	2017-05-19
228732031	832nm	40nm	2017-04-05
228732031	562nm	44nm	2017-04-05
228735255	832nm	40nm	2017-03-10
228735255	562nm	44nm	2017-03-10
228736155	562nm	44nm	2017-04-05
228736155	832nm	40nm	2017-04-05
228739306	562nm	44nm	2017-03-09
228739306	832nm	40nm	2017-03-09
228748383	832nm	40nm	2017-03-18
228748383	562nm	44nm	2017-05-19
228748383	832nm	40nm	2017-05-19

Table 9 continued

Table 9 *(continued)*

EPIC	Filter center [nm]	Filter width [nm]	Obs. Date
228748383	562nm	44nm	2017-03-18
228748826	562nm	44nm	2017-03-09
228748826	832nm	40nm	2017-03-09
228758778	562nm	44nm	2017-04-08
228758778	832nm	40nm	2017-04-08
228758948	832nm	40nm	2017-03-10
228758948	562nm	44nm	2017-03-10
228763938	562nm	44nm	2017-05-19
228763938	832nm	40nm	2017-05-19
228763938	562nm	44nm	2017-03-18
228763938	832nm	40nm	2017-03-18
228801451	832nm	40nm	2017-03-11
228801451	562nm	44nm	2017-03-11
228804845	562nm	44nm	2017-03-10
228804845	832nm	40nm	2017-03-10
228809391	562nm	44nm	2017-03-10
228809391	832nm	40nm	2017-03-10
228809550	832nm	40nm	2017-03-18
228809550	562nm	44nm	2017-03-18
228846243	832nm	40nm	2017-03-17
228846243	562nm	44nm	2017-03-17
228849382	832nm	40nm	2017-05-20
228849382	562nm	44nm	2017-05-20
228888935	832nm	40nm	2017-03-17
228888935	562nm	44nm	2017-03-17
228894622	832nm	40nm	2017-03-09
228894622	562nm	44nm	2017-03-09
228934525	562nm	44nm	2017-03-09
228934525	832nm	40nm	2017-03-09
228964773	562nm	44nm	2017-03-18
228964773	832nm	40nm	2017-03-18
228968232	832nm	40nm	2017-03-18
228968232	562nm	44nm	2017-03-18
228974324	832nm	40nm	2017-03-10
228974324	562nm	44nm	2017-03-10
228974907	562nm	44nm	2017-03-18
228974907	832nm	40nm	2017-03-18
229004835	562nm	44nm	2017-03-11
229004835	832nm	40nm	2017-03-11
229017395	832nm	40nm	2017-03-18
229017395	562nm	44nm	2017-03-18
229103251	832nm	40nm	2017-03-09
229103251	562nm	44nm	2017-03-09
229131722	832nm	40nm	2017-05-19
229131722	832nm	40nm	2017-03-10
229131722	562nm	44nm	2017-05-19
229131722	562nm	44nm	2017-03-10
229133720	562nm	44nm	2017-03-11
229133720	832nm	40nm	2017-03-11

Table 11. Predicted atmospheric characteristics, where g is surface gravity, H is atmospheric scale height, and $\delta_{\rm TS}$ is the expected amplitude of atmospheric spectral features.

EPIC	g [$g_\oplus$]	H [km]	$\delta_{\rm TS}$ [ppm]
201092629.01	1.38	156	94
201102594.01	1.38	128	318
201110617.01	1.92	298	107
201111557.01	1.80	246	73
201127519.01	0.57	575	1146
201128338.01	1.49	96	78
201132684.01	2.08	194	37
201132684.02	1.34	252	98
201164625.01	0.94	1050	55
201166680.01	1.54	285	43
201166680.02	1.62	209	29
201180665.01	0.26	1359	2885
201211526.01	1.80	150	41
201225286.01	1.50	193	85
201274010.01	1.41	214	90
201352100.01	1.32	195	122
201357643.01	0.94	414	152
201386739.01	1.10	377	197
201390048.01	2.09	128	51
201390927.01	1.25	447	169
201392505.01	1.13	180	143
201437844.01	1.46	304	56
201437844.02	0.95	357	122
201595106.01	2.00	396	68
201598502.01	1.63	129	124
201615463.01	1.54	313	35
228707509.01	0.37	854	1850
228720681.01	0.49	641	890
228721452.01	1.08	887	108
228721452.02	1.97	235	50
228724899.01	1.08	393	197
228725791.01	1.57	265	158
228725791.02	1.54	190	117
228725972.01	2.00	213	62
228725972.02	1.44	225	101
228729473.01	0.33	1524	248
228732031.01	1.84	476	190
228734900.01	1.10	348	56
228735255.01	0.45	895	1463
228736155.01	2.01	236	59
228739306.01	1.37	275	109
228748383.01	1.29	348	52
228748826.01	1.41	287	141
228753871.01	1.46	165	86
228758778.01	1.46	127	162
228758948.01	0.97	354	184
228763938.01	1.81	150	51
228784812.01	2.02	240	43
228798746.01	2.12	183	70
228801451.01	2.00	384	95
228801451.02	1.61	197	86
228804845.01	1.69	383	52
228809391.01	1.29	212	89
228809550.01	0.44	1192	1642

Table 11 continued

Table 10. TNG/HARPS-N results.

EPIC	T_{obs} [BJD$_{TDB}$]	RV [km s^{-1}]	BIS [km s^{-1}]	FWHM [km s^{-1}]	log(RHK)	B-V [mag]	T_{exp} [sec]	SNR [5500 nm]
228801451	2457782.629699	22.960809 ± 0.001844	-0.012789	7.175241	-4.5707 ± 0.0098	0.873	1800.0	48.8
201595106	2457782.687224	0.692781 ± 0.002263	-0.022588	6.965865	-4.9714 ± 0.0273	0.703	2400.0	45.0
201437844	2457762.701586	-3.449696 ± 0.005740	0.037015	20.649605	-4.8647 ± 0.0058	0.451	1200.0	101.6
201437844	2457774.738143	-3.441043 ± 0.005931	0.045533	20.699375	-4.8584 ± 0.0060	0.451	1800.0	98.7
201437844	2457774.759707	-3.441611 ± 0.006562	0.073457	20.632207	-4.8629 ± 0.0071	0.451	1800.0	90.0

Table 11 *(continued)*

EPIC	g [$g_\oplus$]	H [km]	δ_{TS} [ppm]
228834632.01	1.76	124	78
228836835.01	1.99	199	188
228846243.01	0.59	655	202
228849382.01	1.91	176	85
228849382.02	1.54	152	97
228888935.01	0.33	1918	1219
228894622.01	1.24	354	288
228934525.01	1.64	185	122
228934525.02	1.60	146	100
228964773.01	0.84	251	227
228968232.01	1.35	267	152
228974324.01	0.97	342	154
228974907.01	1.21	470	26
229004835.01	1.64	191	51
229017395.01	1.22	288	66
229103251.01	1.02	394	127
229131722.01	1.47	229	55
229133720.01	1.51	244	140

Table 12. Comparison of parameters between *K2* pipelines.

EPIC	P_{orb} [days]	ΔP [σ]	R_p [$R_\star$]	ΔR_p [σ]	b	Δb [σ]	a [$R_\star$]	Δa [σ]
201092629.01	$26.809633^{+0.001327}_{-0.001235}$	3.7	$0.0263^{+0.0011}_{-0.0007}$	3.0	$0.25^{+0.28}_{-0.17}$	0.4	$48.0^{+2.0}_{-6.0}$	0.7
201102594.01	$6.513855^{+0.000534}_{-0.000660}$	0.0	$0.0656^{+0.0138}_{-0.0041}$	0.3	$0.54^{+0.37}_{-0.37}$	0.3	$23.0^{+4.3}_{-10.9}$	0.1
201110617.01	$0.813175^{+0.000032}_{-0.000032}$	0.5	$0.0163^{+0.0008}_{-0.0007}$	0.1	$0.39^{+0.33}_{-0.27}$	0.0	$4.6^{+0.5}_{-1.0}$	0.4
201111557.01	$2.302093^{+0.000127}_{-0.000133}$	0.8	$0.0143^{+0.0010}_{-0.0008}$	0.1	$0.40^{+0.34}_{-0.28}$	0.0	$12.0^{+1.5}_{-3.0}$	0.1
201127519.01	$6.178825^{+0.000030}_{-0.000030}$	0.6	$0.1080^{+0.0024}_{-0.0016}$	1.1	$0.24^{+0.15}_{-0.16}$	0.3	$17.7^{+0.4}_{-0.8}$	0.6
201128338.01	$32.652883^{+0.002143}_{-0.002309}$	0.6	$0.0418^{+0.0023}_{-0.0014}$	1.3	$0.40^{+0.32}_{-0.30}$	0.1	$57.0^{+4.8}_{-14.0}$	0.2
201132684.01	$5.898463^{+0.001803}_{-0.001503}$	1.5	$0.0135^{+0.0009}_{-0.0009}$	0.7	$0.30^{+0.23}_{-0.20}$	0.3	$13.3^{+1.3}_{-2.1}$	0.6
201132684.02	$10.062708^{+0.001114}_{-0.001122}$	1.3	$0.0271^{+0.0012}_{-0.0010}$	0.9	$0.43^{+0.22}_{-0.26}$	0.1	$18.9^{+1.9}_{-3.1}$	0.0
201164625.01	$2.713225^{+0.001656}_{-0.001971}$	0.6	$0.0090^{+0.0057}_{-0.0023}$	0.5	$0.47^{+0.37}_{-0.32}$	0.1	$18.8^{+48.6}_{-11.3}$	1.2
201166680.01	$11.540719^{+0.002151}_{-0.002063}$	0.4	$0.0136^{+0.0006}_{-0.0006}$	0.8	$0.43^{+0.16}_{-0.18}$	0.1	$21.0^{+1.0}_{-2.1}$	0.1
201166680.02	$24.942035^{+0.003282}_{-0.003280}$	0.6	$0.0147^{+0.0005}_{-0.0005}$	1.4	$0.22^{+0.26}_{-0.16}$	0.5	$35.0^{+1.7}_{-3.5}$	0.1
201180665.01	$17.773142^{+0.000122}_{-0.000123}$	1.1	$0.1879^{+0.0035}_{-0.0034}$	0.4	$0.67^{+0.02}_{-0.02}$	0.8	$33.6^{+0.5}_{-0.4}$	0.5
201211526.01	$21.073824^{+0.003409}_{-0.002816}$	1.2	$0.0164^{+0.0014}_{-0.0008}$	0.6	$0.40^{+0.35}_{-0.28}$	0.1	$38.0^{+5.9}_{-9.7}$	0.0
201225286.01	$12.420030^{+0.000967}_{-0.000768}$	1.0	$0.0249^{+0.0032}_{-0.0011}$	0.0	$0.40^{+0.37}_{-0.28}$	0.1	$25.8^{+2.2}_{-7.8}$	0.3
201274010.01	$13.008576^{+0.001302}_{-0.001295}$	0.6	$0.0278^{+0.0015}_{-0.0013}$	0.8	$0.42^{+0.34}_{-0.28}$	0.0	$27.7^{+2.9}_{-7.4}$	0.1
201352100.01	$13.383697^{+0.001049}_{-0.001031}$	0.1	$0.0307^{+0.0019}_{-0.0013}$	0.9	$0.41^{+0.33}_{-0.30}$	0.1	$36.4^{+3.6}_{-9.5}$	0.3
201357643.01	$11.893194^{+0.000420}_{-0.000420}$	0.2	$0.0318^{+0.0008}_{-0.0006}$	0.1	$0.36^{+0.32}_{-0.25}$	0.0	$17.7^{+1.1}_{-3.7}$	0.0
201386739.01	$5.768345^{+0.000696}_{-0.000597}$	0.8	$0.0370^{+0.0019}_{-0.0015}$	1.1	$0.38^{+0.29}_{-0.25}$	0.1	$11.2^{+0.9}_{-2.1}$	0.0
201390048.01	$9.456636^{+0.000964}_{-0.000971}$	1.6	$0.0177^{+0.0011}_{-0.0008}$	0.9	$0.43^{+0.34}_{-0.30}$	0.0	$24.3^{+2.7}_{-6.9}$	0.1
201390927.01	$2.637995^{+0.000129}_{-0.000132}$	0.0	$0.0290^{+0.0017}_{-0.0013}$	0.9	$0.44^{+0.32}_{-0.30}$	0.0	$10.6^{+1.2}_{-2.8}$	0.1
201392505.01	$27.363675^{+0.035237}_{-0.016303}$	2.9	$0.0160^{+0.0043}_{-0.0047}$	5.3	$0.56^{+0.32}_{-0.37}$	0.3	$68.6^{+20.6}_{-26.9}$	1.4
201437844.01	$9.553130^{+0.001159}_{-0.001060}$	2.4	$0.0152^{+0.0004}_{-0.0004}$	1.8	$0.22^{+0.26}_{-0.15}$	0.5	$19.4^{+0.9}_{-1.8}$	0.7
201437844.02	$21.057795^{+0.001448}_{-0.001458}$	0.0	$0.0308^{+0.0006}_{-0.0006}$	0.3	$0.40^{+0.16}_{-0.11}$	0.5	$32.9^{+1.5}_{-3.0}$	0.5
201595106.01	$0.877180^{+0.000040}_{-0.000041}$	1.2	$0.0129^{+0.0008}_{-0.0007}$	1.2	$0.42^{+0.32}_{-0.29}$	0.0	$6.1^{+0.8}_{-1.4}$	0.3
201598502.01	$7.514375^{+0.000687}_{-0.000779}$	0.5	$0.0385^{+0.0039}_{-0.0021}$	0.9	$0.45^{+0.36}_{-0.32}$	0.1	$21.9^{+2.8}_{-7.5}$	0.2
201615463.01	$8.527713^{+0.001707}_{-0.001639}$	0.2	$0.0139^{+0.0008}_{-0.0006}$	1.1	$0.41^{+0.31}_{-0.28}$	0.0	$10.9^{+1.0}_{-2.6}$	0.1
228707509.01	$15.349275^{+0.000298}_{-0.000302}$	3.7	$0.1631^{+0.0021}_{-0.0037}$	2.8	$0.68^{+0.04}_{-0.05}$	0.8	$24.1^{+0.8}_{-0.7}$	0.9
228720681.01	$15.781458^{+0.000245}_{-0.000243}$	0.3	$0.1019^{+0.0022}_{-0.0030}$	0.9	$0.74^{+0.04}_{-0.06}$	0.6	$24.3^{+1.7}_{-1.2}$	0.6
228721452.01	$0.505574^{+0.000052}_{-0.000054}$	1.0	$0.0076^{+0.0008}_{-0.0007}$	0.6	$0.74^{+0.10}_{-0.16}$	0.9	$2.9^{+0.2}_{-0.4}$	1.0

Table 12 continued